Trace elements in sulfides from the Maozu Pb-Zn deposit, Yunnan Province, China: Implications for trace element incorporation mechanisms and ore genesis

Zhenli Li[1,2], Lin Ye[1*], Yusi Hu[1,2], Chen Wei[1,2], Zhilong Huang[1], Yulong Yang[3], Leonid Danyushevsky[4]

[1]State Key Laboratory of Ore Deposit Geochemistry, Institute of Geochemistry, Chinese Academy of Sciences, Guiyang 550081, China

[2]University of Chinese Academy of Sciences, Beijing, 100049, China

[3]College of Earth Sciences, Chengdu University of Technology, Chengdu 610059, China

[4]CODES, University of Tasmania, Hobart, Tas. 7001, Australia

ABSTRACT: The Sichuan-Yunnan-Guizhou Pb-Zn metallogenic province (SYGMP) is an important region for Pb-Zn resources in China. However, considerable controversy remains as to whether the Pb-Zn deposits are Mississippi Valley Type (MVT). The Maozu deposit, a typical example of the carbonate-hosted Pb-Zn deposits in the SYGMP, occurs in the late Ediacaran Dengying Formation and its ore bodies are divided into three types: lower layer (LL), vein layer (VL) and upper layer (UL) ore bodies based on the spatial relationship. In this study, laser ablation-inductively coupled plasma-mass spectrometry (LA-ICP-MS) was used to systematically analyze the trace element compositions of sphalerite and galena in these three ore bodies. The results show that sphalerite is characterized by Cd and Ge enrichment; Fe, Mn and Co depletion; and local In and Sn enrichment. Most of these elements likely appear as solid solutions in sphalerite and show a wide variation, which is probably related to the medium- and low-temperature mixing of the ore-forming fluids. The local enrichment of In and Sn has likely attributed to the long-distance migration of ore-forming fluids through In-Sn-bearing volcaniclastic rocks. In *vs* Sn and (Cu + Sb) *vs* (Ag + Ge) show strong correlations and similar element distribution in the mapped images, indicating that these elements may be incorporated into sphalerite via a coupled substitution for Zn as $2\mathrm{In}^{3+} + \mathrm{Sn}^{4+} + 2\square \leftrightarrow 5\mathrm{Zn}^{2+}$ ($\square$ = vacancies) and $4(\mathrm{Cu}^{+} + \mathrm{Sb}^{3+}) + (\mathrm{Ge}^{4+} + 2\mathrm{Ag}^{+}) + 2\square \leftrightarrow 13\mathrm{Zn}^{2+}$. Galena is enriched in Ag and Sb with minor Cd and Se and depleted in Bi, and most of the elements may occur as solid solutions. Ag *vs* Sb in galena displays a strong positive correlation, implying the coupled substitution of $\mathrm{Ag}^{+} + \mathrm{Sb}^{3+} \leftrightarrow 2\mathrm{Pb}^{2+}$. Notably, the majority of the trace element concentrations gradually decrease in the order LL → UL except Fe, Co, Cu and Ge, while Fe, In and Sn in sphalerite and Ag and Sb in galena have the highest concentration in the VL, indicating that the VL is a secondary migration channel for the ore-forming fluids. Furthermore, the trace element compositions of the sulfides in the Maozu Pb-Zn deposit are consistent with the typical MVT deposit (hosted in the carbonate sequence) but are markedly different from sedimentary exhalative (SEDEX), volcanogenic massive sulfide (VMS) and skarn-type deposits. Based on these results, as well as the geological and geochemical characteristics of the deposit, the Maozu Pb-Zn deposit is an MVT deposit.

Keywords: Maozu Pb-Zn deposit, Sulfides, Trace elements, LA-ICP-MS, Mapping, MVT

Introduction

The Sichuan-Yunnan-Guizhou Pb-Zn metallogenic province (SYGMP), located in the southwestern margin of the Yangtze Block, China, is an important region of the South China giant low-temperature metallogenic domain and the major source of Pb-Zn-Ag-Ge in China (Hu and Zhou 2012; Zhou et al. 2013; Zhang et al. 2015; Ye et al. 2016). Approximately 400 Pb-Zn ore deposits and occurrences have been explored in the SYGMP (e.g., Zhang 2008; Wu 2013), most of which are hosted in the late Ediacaran to early Permian carbonate rocks; notably, late Ediacaran and Carboniferous carbonates are the principal host rocks (Wu 2013; Ye et al. 2016). Previous studies have shown that all the Pb-Zn deposits in the SYGMP have striking epigenetic characteristics and share features with typical Mississippi Valley Type (MVT) deposits (Leach et al. 1993, 2005) in terms of mineral assemblages, mineralization types, ore host rocks, wall rock alterations. (e.g., Han et al. 2007; Zhang et al. 2015). However, the ore bodies of the Pb-Zn deposits in the SYGMP are typically characterized by massive, thick veinlets filling open spaces controlled by the structure of the host rock, with high grades of Pb and Zn at generally >20%, such as the Huize (Huang et al. 2004; Han et al. 2007), Maoping (Wei et al. 2015) and Fule (Zhu et al. 2016; Li et al. 2018a, b) Pb-Zn deposits, which present slightly different characteristics from those of typical MVT deposits (Leach et al. 1993, 2005). Accordingly, the genetic types of these Pb-Zn deposits in the SYGMP remain inconclusive (e.g., Huang et al. 2004; Zhou et al. 2013; Zhang et al. 2015; Li et al. 2018b). Several hypotheses for the ore genesis have been proposed in the past two decades, such as a distal magmatic-hydrothermal type related to a Permian Emeishan mantle plume (Xie, 1963; Huang et al. 2004), a sedimentary reworked type (Liu and Lin 1999; Tu, 1984), MVT (e.g., Zhang, 2005; Li, 2016; Li et al. 2018a; Wei et al. 2018a), or a unique Sichuan-Yunnan-Guizhou (SYG) type (Han et al. 2007; Zhou et al. 2013b, 2018a, 2018b).

The Maozu deposit, a typical carbonate-hosted Pb-Zn deposit in the SYGMP, occurs in the Late Ediacaran Dengying Formation and has proven Pb + Zn reserves of ~2 Mt, with average grade of 4.15 wt.% Pb and 7.25 wt.% Zn (e.g., Liu et al. 2009; Zhou et al. 2013; Li et al. 2018). Previous studies mainly focused on the geology (Liu and Lin 1999; He et al. 2006), metallogenic regularity (Chen 2002; Liu 2009) and source of the ore-forming metal (Zhou et al. 2013) in the deposit. Due to the lack of geochemical data, in particular the study of trace elements in sulfide, the ore genesis remains a subject of debate, although the following have been postulated: a) sedimentary reworked type (Zhang et al. 1984; Liu and Lin 1999; Zhang 2013); b) SEDEX-type (Chen 2002; He et al. 2006); c) SYG-type

(Zhou et al. 2013); or d) MVT (Liu 2009). These disparate classifications are confusing for exploration or mining design.

Sphalerite, as the chief mineral in Pb-Zn deposits, contains a variety of useful elements such as Ga (Moskalyk 2003), Ge (Höll et al. 2007), In (Alfantazi and Moskalyk 2003), Cd (Bonnet et al. 2016) and Ag (Cook et al. 2009). Previous studies indicated that trace elements, such as Fe, Mn, Cd, Ge, In, Ga, Se and Te, can be used to ascertain important genetic information and can, to a large extent, be used to classify ore genesis types (Zhang 1987; Cook et al. 2009; Ye et al. 2011, 2012, 2016; Li et al. 2016; Wei et al., 2018a, b). The obvious limitation of bulk analysis of trace elements of sulfide separates is that a sample may include fine-grained sulfide minerals with complex texture from different origins, which is common in the Maozu deposit. However, laser ablation-inductively coupled plasma-mass spectrometry (LA-ICP-MS) can accurately and effectively determine the sulfide trace element concentrations of individual sulfide grains (e.g., Watling et al. 1995; Cook et al. 2009; Ye et al. 2011, 2016), making it possible to discriminate different stages in microscale sulfide grains (Cook et al. 2009; Ye et al. 2011, 2016; George et al. 2015, 2016). Furthermore, time-resolved LA-ICP-MS depth profiling can provide information on whether a given trace element is present within the sulfide matrix or enclosed as micro-inclusions, even in elements at extremely low concentrations (e.g., Cook et al. 2009; George et al. 2015; Bonnet et al. 2016).

In this study, to understand the distribution features and substitution mechanisms of the trace elements in the sulfides from the Maozu Pb-Zn deposit in Yunnan, China, LA-ICP-MS (spot and mapping analyses) was used to determine sphalerite and galena trace element chemistry in the deposit. When combined with the geologic setting, these analyses contribute to the development of a robust deposit model.

1. Geology of the Maozu Pb-Zn deposit

The Maozu Pb-Zn deposit is located in the western Yangtze block and northern SYGMP (Fig. 1). The SYGMP is an important production base of Pb, Zn, Ge and Ag in China, and ~400 Pb-Zn deposits or occurrences (no economic value) have been found in the area. The exposed strata in the area include late Ediacaran to Quaternary strata (Fig. 2), including the late Ediacaran Dengying Formation, one of the chief ore-bearing strata in the region, which is mainly composed of phosphorus-bearing and silicified dolomite. The Cambrian strata consist of phosphorite, sandstone and carbonate rocks. Ordovician strata are composed of sandy shale and argillaceous limestone. Silurian rocks are composed of siltstone and carbonates. The lower Devonian is chiefly composed of sandstone and carbonates, and the upper Devonian is mainly composed of dolostone, which is one of the important ore-hosting strata in the region. The Carboniferous strata are predominantly composed of (siliceous) carbonate rocks, which is another important ore-hosting strata in the region; for example, the world-class Huize Pb-Zn deposit mainly occurs in this Carboniferous strata. The Permian rocks predominantly consist of carbonates and basalts. The Triassic layer is mainly composed of clastic rocks and includes the main coal-bearing strata. The chief composition of the Tertiary and Quaternary rocks is sediments that are exposed in the valley or river areas (Han et al. 2007). The NS-striking faults and anticlines are well developed in this region (Zhang et al. 2006). The principal regional structures are the Anninghe-Lvzhijiang, Mile-Shizhong-Shuicheng, Kangding-Yilian-Shuicheng tectonic belts (Fig. 1), most of which are regional compression thrust faults. The Permian Emeishan flood basalts are among the most widely distributed magmatic rocks in the area.

The Maozu deposit is a representative large-scale Pb-Zn deposit hosted in the late Ediacaran Dengying Formation dolostone in the SYGMP. The deposit is located in a triangular area bounded by the Jinsha River in the north, the Maozu reverse fault in the west and the Choushuijing fault in the southeast (Fig. 3a). Some folds are observed in the ore fields, such as the Ganshulin and Baika synclines and the Hongfadong and Changpo anticlines (Fig. 3a). The rocks in the Maozu ore fields are dominated by late Ediacaran carbonate rocks, Cambrian sediments (black shale, sandstone and limestone) and Permian Emeishan basalts (Fig. 3a, b). The late Ediacaran Dengying Formation is the ore-hosting rock and is structurally controlled by the Maozu thrust fault-fold (Fig. 3a). The Permian Emeishan basalts are widely distributed in the western Maozu thrust fault (Fig. 3).

The ore bodies of the Maozu deposit are strictly controlled by stratigraphy (late Ediacaran Dengying Formation) and lithology (dolostone) and can be divided from shallow to deep into three types: upper layer (UL), vein layer (VL) and lower layer (LL) ore bodies. The VL connects the LL and UL (Fig. 3b), and these layers are characterized as follows: 1) The UL occurs in fine to coarse-crystalline stratiform dolomite that is below the phosphorus-bearing layer (Fig. 4a); the thickness is 15-30 m; predominant minerals are sphalerite, fluorite, and dolomite (Fig. 4a-d), and minor amounts of tetrahedrite (Fig. 4d). 2) The VL ores occur in veinlets within the tectonic fractures (Fig. 4e) formed by ore-bearing hydrothermal fluids filling the cracks on both sides of the syngenetic fault (Gao et al. 2011; Liu et al. 2013); Pb-Zn ores are surrounded by breccias (Fig. 4f), in which the volume of galena in sulfide ore is relatively higher than that of the other two ore body types (He et al. 2006; Liu 2009, Fig. 4g-h), with fluorite, quartz and calcite as the main gangue minerals; the VL is probably a secondary hydrothermal channel for ore-forming fluids (Gao et al. 2011; Liu et al. 2013). 3) The LL occurs in stratoid shape within siliceous dolostone; the ore body thickness varies from 50 to 120 m; the minerals are predominantly sphalerite and quartz (Fig. 4i-l), and minor bitumen occurs around the sulfides (Fig. 4l).

The primary sulfide ores are predominantly by sphalerite and galena, with minor pyrite and tetrahedrite. Gangue minerals consist of dolomite, calcite, fluorite, quartz and bitumen. Ore textures and structures separately include the following: granular, porphyritic and metasomatic (Fig. 4c, d, k); massive, banded (Fig. 4i); and disseminated and veined (Fig. 4e). Wall rock alterations are principally dolomitization and calcitization, which are closely associated with Pb-Zn mineralization.

Based on macro- to microscale geological observations, the paragenesis in the Maozu deposit has been identified. Fine pyrite (Py1) in sphalerite precipitated first (Fig. 4k, l), and the particles of the fine pyrites are small due to replacement by later sphalerite or other sulfides. Under a microscope, the sphalerite is cross-cut by later galena veins (Fig. 4c, k), which also wraps around the coarse pyrite (Py2, Fig. 4k), i.e., the coarse pyrite and galena were formed simultaneously. The edges of the galena are in some cases replaced by later tetrahedrite (Fig. 4d, k). Fluorite is frequently cut by sphalerite and galena veins (Fig. 4g). The Pb-Zn ores are in some cases are cut by calcite veins (Fig. 4b), which may indicate that the calcite (and dolomite) is the last mineral to form in the deposit. Based on the macro- to micro-scale geological observations, the mineralization stages in the Maozu deposit were divided into diagenetic, hydrothermal and supergene stages (Fig. 5), and the simplified mineralization sequence is as follows:

Fine pyrite (Py1) → fluorite (Flu) → sphalerite (Sp) → galena (Gn) + coarse pyrite (Py2) → tetrahedrite (Tet) → quartz (Q) → calcite (Cal) + dolomite (Dol).

2. Analytical method

The sulfide samples were collected from all three types of ore bodies in the Maozu mine area, including 6 samples from the upper layer, 4 samples from the vein layer and 3 samples from the lower layer. The details are listed in Table 1, and the sample locations are shown in Fig. 3b. All samples were prepared as one-inch polished blocks.

LA-ICP-MS spot and mapping analyses of trace elements in sphalerite and galena were performed using the Agilent 7700x Quadrupole ICPMS instrument at CODES (University of Tasmania, Hobart, Australia) coupled with a high-performance RESOlution 193-nm ArF ATL excimer laser ablation system equipped with Geostar software. The diameter of the analytical spot was 30 μm. Trace element analyses of the sphalerite (9 samples, 72 spots) and galena (4 samples, 26 spots) from the three ore bodies (UL, VL and LL) were completed, and an average of 8 spots were analyzed for each sample. Each analysis was performed in the time-resolved mode, which involves sequential peak hopping through the mass spectrum. The laser system was operated at a consistent 5 Hz pulse rate, and the laser energy was typically 2.7 J/cm^2, with a dwell ratio of 3.0 μm/sec. The masses of the following elements were measured: ^{55}Mn, ^{57}Fe, ^{59}Co, ^{60}Ni, ^{65}Cu, ^{66}Zn, ^{72}Ge, ^{75}As, ^{77}Se, ^{107}Ag, ^{111}Cd, ^{115}In, ^{118}Sn, ^{121}Sb, ^{125}Te, ^{205}Tl, ^{208}Pb and ^{209}Bi. The analysis time for each sample was 90 s, including 30-s background with laser off and 60s analysis with laser on. Acquisition time for all masses was set to 0.02 s, with a total sweep time of ~0.6 s. Calibration was performed using STDGL2b-2 (an in-house standard), which is suitable for quantitative analyses in different sulfide matrixes (Danyushevsky et al. 2003, 2011). For more details about the analytical process, please refer to Cook et al. (2009) and Ye et al. (2011).

Each measured values of sphalerite samples were adjusted by the following correction factors (Danyushevsky et al. 2011): Mn 1.46, Fe 1.49, Co 1.51, Ni 1.59, Cu 1.53, As 1.36, Se 1.85, Ag 1.40, Cd 1.50, In 1.45, Sn 1.60, Sb 1.17, Te 1.00, Tl 2.17, Pb 1.37 and Bi 1.33. These correction factors have been established by analyzing sphalerite secondary standards using STDGL2b-2 and reflect the significant elemental fractionation between Zn and the other elements during ablation. The correction factor error is <5% (Cook et al. 2009). Whereas, the measured value of galena did not require correction.

The raw analytical data for each spot analysis were plotted as a line graph, and the integration times for background and sample signal were selected. The counts were then corrected for instrument drift (standards were run every 1½ to 2 hours) and converted to concentration values using known values of Zn in the analyzed sphalerite as an internal standard. Data reduction was undertaken using Zn (640,600 ppm) as the internal standard for sphalerite and Pb (866,000 ppm) for galena.

3. Results

The sphalerite (9 samples, 72 spots) and galena (4 samples, 26 spots) from three ore bodies (UL, VL and LL) of the Maozu Pb-Zn deposits are summarized in Table 1, and the data include the mean, median, median absolute deviation (MAD), minima and maxima for each selected sample. The ranges for each selected element in absolute concentrations are shown in Fig. 6 (sphalerite) and Fig. 8 (galena). Representative time-resolved profiles of given elements are shown in Fig. 9. Complete LA-ICP-MS datasets can be found in Electronic Appendix A.

During the analysis, the areas that are free of obvious inclusions or other features in the sulfides were chosen for the experiment. Flat and irregular (inconsistent with Zn and S profiles) acquisition profiles in the time-resolved depth acquisition profiles likely represent elements distributed as solid solutions and microscale inclusions, respectively. Inclusions were excluded during the data reduction.

3.1 Trace elements in sphalerite

Fe: The *iron* concentrations in the sphalerite of the Maozu deposit range from 698 to 20,570 ppm (median 6273 ppm, n=72), which is the highest trace element content in sphalerite and slightly lower than the *iron* content of the MVT deposit (Cook et al. 2009; Ye et al. 2011, 2016; Yuan et al. 2018) (Fig.

6). The Fe counts in the time-resolved depth acquisition profiles are flat and smooth (Fig. 9a-c). The Fe concentrations of the sphalerite in the VL are the most enriched (Fig. 6, 7c), and the Fe content changes in the order LL → VL → UL, with values of 1555-8156 ppm (median 2257 ppm, n=16) → 4386-20,570 ppm (median 9527 ppm, n=16) → 698-14,752 ppm (median 9257 ppm, n=40), respectively.

Cd: *cadmium* has the second highest measured values in sphalerite with respect to any other element analyzed in this study. Its concentration ranges from 2237-4685 ppm (median 3465 ppm, n=72), which is much higher than the content of by-products extracted from sphalerite (100-900 ppm) and consistent with the Cd content of MVT (Cook et al. 2009; Ye et al. 2011, 2016; Yuan et al. 2018). Cadmium was uniformly distributed in the mapping image (Fig. 10) and appeared as a smooth acquisition profile (Fig. 9a-c). *Cadmium* is negatively correlated with Fe and Mn (Fig. 7a-b). Moreover, the median contents of Cd tend to decrease from the LL to VL to UL at 3945 ppm (n=16) → 3678 ppm (n=16) → 3162 ppm (n=40), respectively.

Cu: The *copper* concentrations are not constant and vary from 9.23 to 2752 ppm, with a median of 334 ppm (n=72). The compositions of Cu in sphalerite are similar to those in MVT (Cook et al. 2009; Ye et al. 2011, 2016; Yuan et al. 2018) (Fig. 6). Although Cu is unevenly distributed in the mapping images and has overlapping enrichment areas with Ge, Sb and Ag (Fig. 10), the acquisition profiles of Cu, Ge, Sb and Ag are parallel to the Zn and S acquisition profile (Fig. 9d). Furthermore, the distribution in the (Cu + Sb) *vs* (Ag + Ge) plot (Fig. 9k) exhibits a strong positive correlation (r=0.80).

Sn: The *tin* concentrations in the Maozu deposit are abnormally enriched compared with those in the typical MVT deposit (Cook et al. 2009) and reach the values observed in skarn and massive sulfide deposits (Cook et al. 2009; Ye et al. 2011) (Fig. 6), which vary from 0.05 to 2192 ppm (median 1.52

ppm, n=71). The Sn concentration range is relatively wide, but the majority of Sn is low and only partially enriched. Sn is positively correlated with In (r=0.82, Fig. 7j, Fig. 10). The acquisition profiles of Sn are analogous with In and parallel to the Zn and S acquisition profiles (Fig. 9c). Sn is most abundant in the VL, and the Sn contents in the LL, VL and UL vary from 0.06-14.5 ppm (median 0.25 ppm, n=16), 0.1-2192 ppm (median 54.8 ppm, n=16) and 0.05-179 ppm (median 1.67 ppm, n=39), respectively.

In: The *indium* concentrations in sphalerite of different deposit types vary as shown in Fig. 6. The skarn and massive sulfide deposits (Cook et al. 2009; Ye et al. 2011) contain the highest volume of In, whereas low In contents was observed in the MVT (Fig. 6; Cook et al. 2009; Ye et al. 2011, 2016; Yuan et al. 2018). In concentration in Maozu extend from 0.001 pp to 1191 ppm, with a median of 2.84 ppm (n=66). A remarkable feature is that the maximum concentration of In in the Maozu deposit has reached the levels observed in typical skarn and massive sulfide deposits (Cook et al. 2009; Ye et al. 2011), which are much higher than the In levels of the MVT. Additionally, In and Sn show the same element enrichment areas (Fig. 10). The acquisition profile of In is smooth and parallel to Sn, Zn and S on the time-resolved depth profiles (Fig. 9c). Similar to Sn, In is most enriched in the VL (Fig. 6, Fig. 7j); the variation of In is in the order LL → VL → UL, with values of 0.01-464 ppm (median 0.94 ppm, n=13) → 0.001-1191 ppm (median 35.7 ppm, n=15) → 0.01-397 ppm (median 1.40 ppm, n=38), respectively.

Sb: The *antimony* content is relatively low in the skarn and massive sulfide deposits but those in typical MVT deposits relatively high (Cook et al. 2009; Ye et al. 2011) (Fig. 6). The composition of Sb in the sphalerite of the Maozu deposit is 0.35-835 ppm (median 36.3 ppm, n=71), and it presents a wide variation range and a nonuniform distribution. As previously described, Sb has the same enrichment characteristics as Cu, Ge and Ag (Fig. 10), and these elements have a strong positive correlation (r=0.83, Fig. 7h, k-m). The profile of Sb is smooth and parallel to Cu, Ge, Ag, Zn and S (Fig. 9d).

Pb: The *lead* content shows an uneven enrichment in the mapping image (Fig. 10), and the concentrations are within the range of 0.62-399 ppm (median 8.22 pm, n=72). The ragged and irregular profiles (Fig. 9b) imply that Pb is present as micro-inclusions in sphalerite rather than as a solid solution. Pb and As have similar profiles.

Ge: The *germanium* content ranges widely from 0.30-342 ppm (median 36.9 ppm, n=72), and the Ge concentrations within sphalerite from the Maozu deposit are consistent with those in the MVT (Cook et al. 2009; Ye et al. 2011, 2016; Yuan et al. 2018) while low levels observed in typical skarn (Cook et al. 2009; Ye et al. 2011) and massive sulfide deposits (Cook et al. 2009 and references therein; Ye et al. 2011). The spectrum of Ge is smooth (Fig. 9b, d). Ge shares similar enrichment areas with Cu, Sb and Ag in the mapping images and is positively correlated with these elements (Fig. 7e, h, k).

As: The *arsenic* content in the sphalerite of Maozu varies from 0.75 to 275 ppm (median 9.36 ppm, n=58), which is more enriched than that in the skarn (Cook et al. 2009; Ye et al. 2011) and massive sulfide deposits (Cook et al. 2009 and references therein; Ye et al. 2011) but similar to the concentration in the MVT deposits (Fig. 6). Most of As show smooth LA-ICP-MS down-hole spectral profiles, but several anomalous LA-ICP-MS time-resolved signal spectra (Fig 9d) could be observed which consistent with that of Pb. In the mapping images, *Arsenic* also shows a relatively concordant distribution with Pb.

Ag: The *silver* concentrations range from 1.34-254 ppm (median 12.5 ppm, n=72), and a certain amount of Ag was found in all samples. The Ag contents in the deposits with different genesis types are similar (Fig. 6). Although Ag is unevenly distributed in the mapping images (Fig. 10), the Ag enrichment areas are consistent with the enrichment areas of Cu, Ge and Sb (Fig. 10). In addition, all spot analyses show that Ag show a positive correction with the Cu (r=0.59, Fig.7f), Ge (r=0.48, Fig.7g) and Sb (r= 0.76), respectively.

Mn: The *manganese* content presents a relatively narrow distribution range (Table 1, Fig. 6), with concentrations from 2.78-206 ppm (median 74.5 ppm, n=72). The Mn contents gradually increased from the center to the edge of the sphalerite particles in the mapping image (Fig. 10). The concentration of Mn is generally consistent with that of the MVT deposits but significantly lower than that of the massive sulfide and skarn deposits.

Co: *Cobalt* concentration varies 3 orders of magnitude, ranging from 0.04 ppm to 35.1 ppm (median 4.59 ppm, n=71), which is slightly higher than that of the MVT deposits (Fig. 6). A positive correlation between Co and Ni was observed in Fig. 7d, and Co show coordination changes between Co and Fe (Fig. 10). From the LL to UL, Co shows a trend of gradual enrichment (Fig. 7d). In the profiles, Co presents a flat and smooth acquisition profile that is nearly parallel to Fe.

Ni: The *nickel* concentrations are relatively low, with most below the detection limit, and the maximum is only 3.08 ppm and medians are lower than the concentrations in the massive sulfide and skarn-type sphalerites (Fig. 6). Due to the low contents, the Ni acquisition profiles cannot be shown in the LA-ICP-MS profiles. However, Ni is evenly distributed in the mapping image of sphalerite (Fig. 10). Co and Ni have a strong positive correlation (Fig. 7d).

Se: The *selenium* concentration in sphalerite from the Maozu deposit is mostly lower than the detection limit, and the maximum content is only 3.52 ppm, which is analogous to the concentrations in the MVT and lower than that in the skarn deposits (Fig. 6).

In addition, the concentrations of other elements, such as Te, Tl and Bi, from the Maozu deposit have been detected in a few spots with the contents mostly below the detection limits (Appendix A).

Although the Hg acquisition profile is obvious in the measured samples (Fig. 9a), an accurate Hg value cannot be obtained because there is no available sample standard.

3.2 Trace elements in galena

Sb: *Antimony* is the most enriched element in galena of the Maozu deposit (Fig. 8b), ranging from 342 to 1033 ppm (median 724 ppm, n=26). Sb and Ag are positively correlated (Fig. 7n) and both show smooth LA-ICP-MS acquisition profiles (Fig. 9e-f). Sb contents gradually increase from the LL (498 ppm, n=7) to the UL (740 ppm, n=6), with the highest concentration in the VL ore body (764 ppm, n=13).

Ag: *Silver* is widely distributed in galena of the Maozu deposit (Fig. 8a), ranging from 293-910 ppm (median 582 ppm, n=26). There is a very strong positive correlation between Ag and Sb (r=0.98, n=26; Fig. 7n). In the time-resolved depth acquisition profiles, Ag and Sb appear as flat acquisition profiles that are parallel to the Pb and S (Fig. 9e-f). From the LL (median 426 ppm, n=7) to the UL (median 575 ppm, n=6), Ag gradually increases, and the content of Ag in the VL (median 666 ppm, n=13) is the highest (Fig. 8a).

Se: *Selenium* is relatively enriched in the galena of the Maozu deposit from 0.44-96.4 ppm (median 56.6 ppm, n=22). Although Se is widely distributed (Fig. 8h), Se appears in a flat acquisition profile in the time-resolved depth acquisition profiles (Fig. 9f).

Cd: *Cadmium* is relatively enriched and concentrated in the galena from the Maozu deposit and presents a normal distribution (Fig. 8c) from 19.7-56.7 ppm (median 36.1 ppm, n=26). The Cd acquisition profile is smooth and flat and parallel to Pb and S. The Cd of galena from the three ore bodies shows no obvious differences.

Sn: *Tin* content in galena is relatively low, with most concentrations <10 ppm, and the variation range is 0.61-16.6 ppm (median 2.74 ppm, n=26). From the LL to VL to UL, the median contents change from 0.76 ppm (n=7) to 5.29 ppm (n=13) to 2.33 ppm (n=6), respectively, and the highest Sn concentration occurs in the VL.

Bi: *Bismuth* content in galena is mostly <10 ppm (Fig. 8f), and it ranges from 0.01-14.2 ppm (median 0.48 ppm, n=26). The Bi acquisition profile is smooth and flat and parallel to the Pb and S acquisition profiles (Fig. 9f). The correlation between Bi and Sb is strong (Fig. 7o).

Tl: *Thallium* is the most concentrated trace element in the galena of the LL (Fig. 8e), and the total content range is 4.73-8.59 ppm (median 5.76 ppm, n=26). The acquisition profile of Tl is smooth and flat (Fig. 9e-f). From LL → VL → UL, the median content changes from 8.15 ppm (n=7) → 5.17 ppm (n=13) → 5.84 ppm (n=6), respectively.

Cu: *Copper* is present in relatively low concentrations except in the LL, where its concentration is relatively high (Fig. 8d). The Cu concentrations in the VL and UL are all <1 ppm, and the total distribution range is 0.15-3.04 ppm (median 0.67 ppm, n=24). The correlation between Cu and Tl is strong (Fig. 7o).

In addition, other elements in the galena from the Maozu deposit, such as Fe, Mn, and As, are generally below the minimum detection limit.

4. Discussion

4. 1 Occurrence and substitution mechanisms of trace elements

LA-ICP-MS analysis could provide significant information for the occurring of a particular element. Micro-inclusions are commonly noted in the LA-ICP-MS acquisition profiles (peak) if they are sufficiently large (e.g., Cook et al. 2009; Ye et al., 2011, 2016; George et al. 2015), whereas lattice-bound trace elements and nanoparticles would present flat in the signal spectra and thus hard to distinguish (e.g., Gregory et al. 2014, 2015). In those cases, trace element mapped images may provide additional constrain on the occurring of the elements in hosted minerals. But the hypothesis that these elements occurs as nanoparticles could not be ruled out.

4.1.1 The occurrence of trace elements in sphalerite

Although trace elements of Mn, Cd, Fe and Co show highly variation (Table 1, Fig. 6), these trace elements occur as smooth and flat and follow changes of Zn and S in the LA-ICP-MS acquisition profiles (Fig. 9a). Moreover, these elements are uniformly distributed in the trace element mapping images (Fig. 10), suggesting that these elements likely mainly occur as solid solutions in sphalerite. Notably, in the mapping images (Fig. 10), from the center to the edge of the sphalerite particles, Mn contents gradually increase, probably because the later formation of hydrothermal dolomite contained a certain amount of Mn. Additionally, several spot-like concentration areas enriched Fe and Co are evenly distributed in the mapping images (Fig. 10), which may be attributed to the disseminated pyrite in the sphalerite (Fig. 4k, 10a) and indicates that the Co enrichment is related to the Fe distribution.

The concentrations of elements In, Sn, Cu, Ge, Sb and Ag vary widely (Fig. 6), and these trace elements are unevenly distributed in the mapping images. However, the element acquisition profiles are flat and smooth, which is consistent with the Zn and S acquisition profiles (Fig. 9c, d), implying that these elements did not exist as micro-inclusions. In, Sn and Cu, Ge, Sb, and Ag have overlapping element enrichment areas in the mapping images (Fig. 10), suggesting that these elements may enter into the sphalerite crystal structure by coupled substitution.

The sphalerite contains measurable concentrations of Pb and As, which typically vary greatly (Fig. 6) and are unevenly distributed in the mapped images (Fig. 10). Several acquisition profiles appear as ragged and irregular in the time-resolved profiles and show a coordination change with the profile of

Pb (Fig. 9d), suggesting partly Pb and As exist in sphalerite as micro-inclusions.

The concentrations of Bi, Tl, Ni, Se and other trace elements are extremely low (< 5 ppm), and the acquisition profiles of these elements could not be reflected in the LA-ICP-MS profiles.

4.1.2 The occurrence of trace elements in galena

Although the Ag and Sb concentrations vary widely, these element spectral profiles present smooth and flat and are parallel with the Pb and S in the time-resolved profiles (Fig. 9e-f), which may indicate that Ag and Sb likely enter into the galena crystal structure. Meanwhile, Cd, Se Bi and Tl appear as smooth and flat profiles, which is consistent with the changes in the Pb and S (Fig. 9e, f), revealing that these elements may also occur as solid solutions in galena.

4.1.3 Substitution mechanisms

Many studies have demonstrated that the bivalent cations (e.g., Cd^{2+}, Fe^{2+}, Mn^{2+}, Co^{2+}) are easily incorporated into sphalerite via simple substitution of Zn^{2+}, due to the similar ion radii (Johan 1988; Cook et al. 2009). Tri- and tetravalent elements (e.g., Ge^{4+}, Sb^{4+}, In^{3+}) are thought to enter sphalerite via coupling with monovalent elements (Cu^{+}, Ag^{+}) or through the creation of vacancies (e.g., Bernstein 1986; Cook et al. 2009; Ye et al. 2011; Belissont et al. 2014; Wei et al. 2019). Johan (1988) proposed a general coupled substitution mechanism for trivalent and tetravalent elements in sphalerite as follows:

$$(x + 2y)\, M^{+} + y\, M^{2+} + x\, M^{3+} + y\, M^{4+} \leftrightarrow (2x + 4y)\, Zn^{2+}$$

where M^{+}=Ag, Cu; M^{2+}=Cu, Fe, Cd, Hg, Zn; M^{3+}=In, Ga, Fe, Tl; M^{4+}=Ge, Sn, Mo, W; and x and y are atomic proportions of M^{3+} and M^{4+}, respectively. However, substitution mechanisms these elements still debated. For example, some authors proposed the intake of Ge^{2+} in sphalerite via direct substitutions ($Zn^{2+} \leftrightarrow Ge^{2+}$) (e.g., Cook et al. 2009; Ye et al. 2011). In contrast, Cook et al. (2015) postulated that Ge enters sphalerite lattice through the creation of vacancies such as $2Zn^{2+} \leftrightarrow Ge^{4+} + \square$.

Wei et al. (2019) considered that Cu and Ge show a coupled substitution of Zn ($3Zn^{2+} \leftrightarrow 2Cu^{+} + Ge^{4+}$) due to the correlation between Ge and Cu with a trend to parallel to the molar ratio $(Cu/Ge)_{mol} = 2$.

The atomic ratio (AR) was an effective method to understand the substitution mechanisms of trace elements in sphalerite (e.g., Johan 1988; Belissont et al. 2014; Wei et al. 2019). Therefore, it was applied to determine the substitution of the tri- and tetravalent elements in sulfide from Maozu. Based on the research results of Johan (1988), the slope (k) of different Ars is determined according to the weight ratio (WR) (Mx/My) of the elements to make a line (Fig. 7i) with different Ars (i.e., different slopes). Even in different coordinate systems, the slope (k) is constant due to the constant WR; therefore, the AR is also constant. The AR of each element in the substitution reaction can be determined according to the slope of the regression line in the correlation plot (Fig. 7i). The premise of the application of this plot (Fig. 7i) is that Mx and My have a good linear relationship, basically presenting a linear distribution (e.g., Fig. 7j-o), and the contents of elements are concentrated and cannot be scattered (Fig. 7e-h); otherwise, the calculated AR is not accurate.

As noted above, although In and Sn are not evenly distributed in sphalerite, these elements have similar element distribution features in the mapped images and show a good linear relationship in Fig. 7j (r=0.82, n=66), indicating that these elements are coupled substitutions for Zn in sphalerite, a similar result has been reported by Belissont et al. (2014). Other than In and Sn, there may be the presence of vacancies (represented by □) for other uncertain elements. According to the equation of Johan (1988), the possible substitution equation is $xIn^{3+} + ySn^{4+} + z\square \leftrightarrow (x + y + z)\,Zn^{2+}$.

As the plots are concentrated and linearly distributed in the In-Sn correlation plot, the regression line (r=0.82, k=0.6) is approximately parallel to In/Sn=2/1 (k=0.5) (Fig. 7j). The slope of the regression line is slightly higher than the slope of the line with an AR of 2/1, which is attributed to the existing vacancies (□). The atomic ligand ratio of In^{3+} and Sn^{4+} is 2/1; therefore, the most likely coupled substitution is $2In^{3+} + Sn^{4+} + 2\square \leftrightarrow 5Zn^{2+}$.

2) Cu, Ge, Ag, and Sb have consistent element distribution characteristics in the mapping images, and (Cu + Sb) *vs* (Ag + Ge) (r=0.8, n=72, Fig. 7k) show strongly positive correlation, therefore these characteristics reveal that the elements are incorporated into sphalerite by coupled substitution. In the correlation plots of Cu *vs* Ge (Fig. 7e), Cu *vs* Ag (Fig. 7f), Ge *vs* Ag (Fig. 7g) and Sb *vs* Ge (Fig. 7h), the corresponding plots are scattered or not linearly distributed; thus, the AR cannot be determined. Although the correlation coefficients of (Cu + Sb) *vs* (Ag + Ge) reached 0.8 (n=69) and 0.98 (n=3), there are two groups of linear relations (Fig. 7k), which suggested that other metal atoms (vacancies) may participate in the substitution; therefore, the AR cannot be determined by these plots.

The plots of Cu *vs* Sb (r=0.73, k=1.11, Fig. 7l) and Sb *vs* Ag (r=0.76, k=0.47, Fig. 7m) are concentrated and linearly distributed, and their slopes are approximately parallel to those of the AR, at 1/1 (k=1) and 2/1 (k=0.5), respectively. The atomic ratio of Cu/Sb is 1/1 and that of and Sb/Ag is 2/1. According to the equation of Johan (1988), Ge is tetravalent and Ag is monovalent. Belissont et al. (2014) reported Sb is trivalent and Cu is monovalent, in agreement with the results of AR. As noted above, other uncertain atoms (vacancies) may participate in the substitution, which may cause the coupled substitution of these elements (Cu, Ge, Ag, and Sb) to be slightly different from the equation of Johan (1988). Consequently, the possible coupled substitution is $4(Cu^{+} + Sb^{3+}) + (Ge^{4+} + 2Ag^{+}) + 2\square \leftrightarrow 13Zn^{2+}$.

Regarding galena, the contents of Ag and Sb vary greatly (Fig. 8a-b). Conventionally, many researches on galena have principally focused on elements with high concentrations, such as Ag, Sb and Bi (Van Hook 1960; Jeppsson 1989; Lueth et al. 2000; Chutas et al. 2008; Renock and Becker

2011). *Thallium* is more readily incorporated into the crystal lattices of galena with Bi, Ag and Sb by coupled substitution due to the existence of Cu (George et al. 2015). Although all these elements have good linear relationships (r=0.98, n=26) in the correlation plots of Ag *vs* Sb (Fig. 7n) and (Bi + Sb) *vs* (Cu + Ag + Tl) (Fig. 7o), the coupled relationship of Ag and Sb is only considered because of the low contents of Bi, Cu and Tl in galena from the Maozu deposit. The regression line slope of Ag *vs* Sb (k=0.97, Fig. 7n) is close to 1 (AR is 1/1), (Ag/Sb) at=1/1. Additionally, previous studies generally proposed Ag as monovalent and Sb as trivalent (Renock and Becker 2011; George et al. 2015; Ye et al. 2016). Hence, the coupled substitution between Ag, Sb and Pb may be simplified as $Ag^{+} + Sb^{3+} \leftrightarrow 2Pb^{2+}$.

4.2 Mineralization temperature

Many studies have indicated that trace elements in sphalerite have a close connection with the temperature during sulfide precipitation; therefore, the contents of trace elements in sphalerite can indicate the temperature of mineral formation (Oftedahl 1940; Moller 1987; Mladenova and Valchev 1998; Kelley et al. 2004; Frenzel et al. 2016). Conventionally, sphalerite enriched in Fe, Mn, In, Sn, and Te indicate sulfide formation under a high-temperature condition, while sphalerite formed at low temperature is enriched in Cd, Ga and Ge with a low In/Ge ratio (Ye et al. 2016). Sphalerite in the Maozu deposit is characterized by the enrichment of Cd and Ge and depletion of Fe, Mn, Co, Se and Te. Fe content (698.1-20,570 ppm) in sphalerite from the Maozu deposit is similar to the Fe content (0.6-4.2 wt %) in sphalerite formed at 100-200 °C according to Kelley et al. (2004). The compositions of the trace elements in sphalerite from the Maozu Pb-Zn deposit show enrichment of low-temperature elements, such as Cd and Ge, which are consistent with those in the typical MVT Pb-Zn deposits (Cook et al. 2009; Ye et al. 2011) (Fig. 6).

Cao et al. (2014) showed that sphalerite formed at a high temperature (200-355 °C), the color of sphalerite is dark and rich in Fe (3.58%-11.42%) and Mn (0.2%-0.4%). While sphalerite formed at a low temperature (110-180 °C) is lighter and relatively depleted in Fe (0.23%-2.0%) and Mn (0.003%-0.05%). The colors of the sphalerite in the Maozu Pb-Zn deposit are dominated by brown and yellow (Fig. 4a, e, j). The contents of Fe and Mn are 0.07%-2.1% and ~0.02%, respectively, which are similar to the contents of Fe and Mn in low-temperature sphalerite. These characteristics indicate that the mineralization temperature of the sphalerite in the Maozu Pb-Zn deposit is mainly medium to low temperature.

Frenzel et al. (2016) demonstrated that the trace element concentrations (Ga, Ge, In, Fe, Mn, Ag, Co and Cu) of sphalerite can be used to calculate the formation temperature. Because our experiment did not analyze the content of Ga, we use the Ga content (~20 ppm, Ye et al. 2011) from the Huize deposit (a typical Pb-Zn deposit in SYGMP that is similar in geological and geochemical features to the Maozu deposit) as a proxy according to the data from Frenzel et al. (2016). As a result, the formula (Frenzel et al. 2016) for calculating the ore-forming temperature of sphalerite was used, and the considered trace elements were Fe, Ge, In and Mn from this paper and Ga from Huize. The calculated ore-forming temperature of sphalerite in the Maozu deposit is 120.5-288.7 °C (average 179.3 °C), which is similar to a previous analysis of fluid inclusions in the Maozu deposit (140-280 °C, Yang et al. 2017), revealing that the ore-forming fluids of the deposit are medium-low temperature fluids.

In addition, the concentrations of In and Sn in the VL are the highest (Fig. 6, 7j), and relatively more galena occurs in the VL than in the LL and UL (Fig. 4). These characteristics may indicate that the VL is the secondary channel for the migration of ore-forming fluids. The concentrations of Fe, In, and Sn in sphalerite and Ag and Sb in galena are the most enriched in the VL (Fig. 6). This finding may suggest that ore-forming fluid migration occurs from deep to shallow and that the VL connects the UL and LL by tectonic fracture zone and is the secondary migration channel of the ore-forming fluids.

4.3 Ore genetic type

The sulfide ore bodies of the Maozu deposit mainly occurs as stratiform and lentiform bodies, resulting in some researchers consider it as a sedimentary reworked type or SEDEX-type of deposit (e.g., Chen et al. 2002; He et al. 2006). In fact, the ore-hosting rock is the late Ediacaran Dengying Formation dolostone, which differs from the host rocks (siliciclastic rocks) of the SEDEX-type. Moreover, the steeply VL has been discovered with the mining exposures (Fig. 4), suggesting that the Maozu deposit shows clear epigenetic origin. Furthermore, George et al (2015) found that galena from the SEDEX Pb-Zn deposit is enriched in Bi (>100 ppm, up to 1000 ppm), but Bi in galena from the Maozu deposit is normally below 1 ppm. In plots of Fe *vs* Mn, Fe *vs* Bi, Mn *vs* Bi and Ag *vs* Bi (Fig. 11), the trace elements in galena of the Maozu deposit plot away from those of the SEDEX deposits (George et al. 2015, 2016; Ye et al. 2016). Therefore, we consider that the Mazu deposit is unlikely attributed to a syngenetic origin.

Previous studies have suggested that the Maozu deposit is characterized by: (1) stratiform and dipping vein ore bodies hosted in the Late Ediacaran Dengying Formation dolostone; (2) relatively simple mineral assemblage, and including sphalerite, galena, dolomite, and minor pyrite and quartz; (3) ore-forming fluids with low-medium temperature (140-280°C) and medium-high salinity (10-18 wt.% NaCl eqv.)(Yang et al. 2017); (4) a mixing metal source of metamorphic basement rocks and ore-hosting sedimentary rocks (Zhou et al. 2013); (5) sulfur from a thermochemical reduction the ore-hosting sulfate (Zhou et al. 2013). All these geological features are consistent with those of typical MVT deposits (Leach et al. 1993, 2005).

Trace elements in sphalerite, such as Fe, Mn, Cd, Ge, In, Ga, Se and Te, has been used to classify the deposit genesis in recent decades because trace elements can be used to provide genetic information (Zhang 1987; Cook et al. 2009; Ye et al. 2011, 2012, 2016; Wei et al. 2018a, b). In general, the MVT Pb-Zn deposit is enriched in Cd, Ge, and Ga (Ye et al. 2011; Bonnet et al. 2016; Yuan et al. 2018) and depleted in Fe, Mn, In, Sn, and Co (Ye et al. 2011, 2016; Wei et al. 2018a). The massive sulfide deposits (SEDEX and VMS) are characterized by enrichment in Fe, Mn, and In and depletion in Cd, Ge, and Ga (Cook et al. 2009; Ye et al. 2011; Wei et al. 2018b). The skarn-type deposits are enriched in Mn and Co and depleted in In, Sn and Fe (Cook et al. 2009; Ye et al. 2011). For the Maozu deposit, trace element compositions in sphalerite are characterized by depletion in Fe, Mn, and Co. The Mn and Co contents in sphalerite from the Maozu deposit are lower than that of the skarn-type (most of Mn >1000 ppm and Co >200 ppm, Table 2) (Cook et al. 2009; Ye et al. 2011), and the Fe and Mn contents are significantly lower than those in the sedimentary exhalative deposit (most of Fe and Mn >1000 ppm, Table 2) (Ye et al. 2011). Whereas, these sphalerite samples are enriched in Cd and Ge which are analogous to those of MVT deposits from the USA, China and Mexico (Cook et al. 2009; Ye et al. 2011; Bonnet et al. 2016; Wei et al. 2018a). Furthermore, in the binary plots of different genesis deposits (Fig. 12), including Mn *vs* Fe, Mn *vs* Co, Mn *vs* Ge and Cd/Fe *vs* Mn, all the samples fall into the MVT range.

In conclusion, the composition of trace elements in sulfides from the Maozu Pb-Zn deposit is significantly different from that of the sedimentary exhalative and skarn-type deposits but consistent with that of the MVT deposits (Cook et al. 2009; Ye et al. 2011, 2016; Wei et al. 2018a, b). Combined with the geological and geochemical characteristics of the deposit, we propose that the deposit is an MVT deposit.

4.4 A possible reason for anomalies Indium and Tin in sphalerite

Generally, the magma-related deposits show high In and Sn concentrations in sphalerite (e.g., Cook et al. 2009; Belissont et al. 2014; Wei et al. 2018b). Most of the Pb-Zn deposits in the SYGMP are considered as MVT that have no genetic relationship with igneous rock (Leach et al. 2005). Therefore, the concentrations of In and Sn in these deposits are very low (most <10 ppm, Fig. 6). However, several LA-ICP-MS spot analyses in this study display high concentrations of In and Sn. Interestingly, Mo et al. (2013) found that the volcanic rocks in the basement (the main metal source of these Pb-Zn deposits in the SYGMP) contain high level of In (78 ppm) and Sn (120 ppm). Meanwhile, the mineralizing fluids of MVT deposits are defined as a long-distance migration of basinal fluid (Garven, 1985, Garven and Raffensperger, 1997). Therefore, a possible explanation is that the hydrothermal fluid flow through the basement including In-Sn-bearing volcanic rocks and leach metals out, and final form in In-Sn-bearing sphalerite because In and Sn preferred host in sphalerite (Höll et al. 2007; Cook et al. 2009). But this hypothesis should be verified in the future.

5. Implications

To understand the genesis of Pb-Zn deposits in the SYGMP, the trace elements in different sulfides (sphalerite and galena) from the Maozu Pb-Zn deposit, which is a representative Pb-Zn deposit in the SYGMP, were analyzed by LA-ICP-MS. Compared with trace elements in sulfides from the different genetic type Pb-Zn deposits, the Maozu Pb-Zn deposit is characterized by enrichment of Ge, Fe, Mn, Co in sphalerite and Ag, Sb, Cd, Se in galena, which is similar to the composition of typical MVT deposits and different from those of SEDEX, VMS, and skarn-type Pb-Zn deposits, suggesting that the Maozu deposit is an MVT deposit.

The occurrence of the trace elements in sulfides were determined by the LA-ICP-MS acquisition profiles, mapped images and element inter-correlation. Bivalent cations such as Mn, Cd, Fe, and Co likely enter sphalerite lattice via a direct substitution. Tri- and tetravalent elements including In^{3+}, Sn^{4+}, Ge^{4+} and Sb^{3+} were incorporated into sphalerite by coupling with monovalent elements (Cu+, Ag+) as $2In^{3+} + Sn^{4+} + 2\square \leftrightarrow 5Zn^{2+}$ ($\square$ = vacancies) and $4(Cu^{+} + Sb^{3+}) + (Ge^{4+} + 2Ag^{+}) + 2\square \leftrightarrow 13Zn^{2+}$. Partly Pb and As exist in sphalerite as micro-inclusions. In addition, strong binary correlations between Sb and Ag in galena imply the coupled substitution of $Ag^{+} + Sb^{3+} \leftrightarrow 2Pb^{2+}$.

The enrichment of trace elements in sulfide minerals differs among the lower layer (LL), vein layer (VL) and upper layer (UL). In sphalerite, Fe, Co, Cu, and Ge show a slight decrease trend while Cd, Mn, Ag, Sb, and Pb display a gradually increasing trend from the upper to lower layer. Notably, Fe, In and Sn in sphalerite and Ag and Sb in galena are the highest in the VL, suggesting that the VL is a secondary migration channel of the ore-forming fluids.

Acknowledgments

This research project was jointly supported by the National Natural Science Foundation of China (Grant No. 41673056, 41430315), the National Key R&D Program of China (No. 2017YFC0602502), and the National ‘973 Project’ (No. 2014CB440906). We would like to thank Dr. Ivan Belousov, Dr. Paul Olin, Dr. Sarah Gilbert (CODES, University of Tasmania) for their assistance in LA-ICPMS analysis. Associate Editor Daniel Gregory, and two anonymous reviewers are thanked for their constructive comments and suggestions.

Reference

Alfantazi, A.M., and Moskalyk, R.R. (2003) Processing of indium: a review. Minerals Engineering, 16, 687–694.

Bellissont, R., Boiron, M.C., Luais, B., and Cathelineau, M. (2014) LA-ICP-MS analyses of minor and trace elements and bulk Ge isotopes in zoned Ge-rich sphalerites from the Noailhac – Saint-Salvy deposit (France): Insights into incorporation mechanisms and ore deposition processes. Geochimica et Cosmochimica Acta, 126, 518–540.

Benzaazoua, M., Marion, P., Pinto, A., Migeon, G., and Wagner, F.E. (2003) Tin and indium mineralogy within selected samples from the Neves Corvo ore deposit (Portugal): a multidisciplinary study. Minerals Engineering, 16, 1291–1302.

Bernstein, L.R. (1985) Germanium geochemistry and mineralogy. Geochimica et Cosmochimica Acta, 49(11), 2409–2422.

Bernstein, L.R. (1986) Geology and mineralogy of the APEX germanium–gallium mine, Washington County, Utah. USGS Bull, 1577, 1–9.

Bonnet, J., Mosser, R.R., Caumon, M.C., Rouer, O., Andre, M.A.S., Cauzid, J., and Peiffert, C. (2016) Trace element distribution (Cu, Ga, Ge, Cd, and Fe) in sphalerite from the Tennessee Mvt deposits, USA, by combined EMPA, LA-ICP-MS, raman spectroscopy, and crystallography. Canadian Mineralogist, 54(5), 1261–1284.

Cao, H.W., Zhang, S.T., Zheng, L., Liu, R.P., Tian, H.H., Zhang, X.H., and Li, J.J. (2014) Geochemical characteristics of trace element of sphalerite in the Zhongyuku (Pb)-Zn deposit of the Luanchuan, Southwest of China. Journal of Mineral Petrol, 34(3), 50–59 (in Chinese with English abstract).

Chen, Q.L. (2002) Metallogenetic geological features and ore guides of high-grade Pb-Zn deposits in Yuhucun formation，northeast Yunnan．Geology Prospecting, 38(1), 22－26 (in Chinese with English abstract).

Chutas, N.I., Kress, V.C., Ghiorso, M.S., and Sack, R.O. (2008) A solution model for hightemperature

PbS-AgSbS2-AgBiS2 galena. American Mineralogist, 93, 1630–1640.

Cook, N.J., Ciobanu, C.L., Brugger, J., Etschmann, B., Howard, D.L., De Jonge, M.D., Ryan, C., and Paterson, D. (2012) Determination of the oxidation state of Cu in substituted CuIn-Fe-bearing sphalerite via l-XANES spectroscopy. American Mineralogist, 97, 476–479.

Cook, N.J., Ciobanu, C.L., Pring, A., Skinner, W., Shimizu, M., Danyushevsky, L., Saini-Eidukat, B., and Melcher, F. (2009) Trace and minor elements in sphalerite: A LA-ICPMS study. Geochimica et Cosmochimica Acta, 73, 4761–4791.

Cook, N.J., Etschmann, B., Ciobanu, C.L., Geraki, K., Howard, D.L., Williams, T., Rae, N., Pring, A., Chen, G.R., Johannessen, B., and Brugger, J. (2015) Distribution and substitution mechanism of Ge in a Ge-(Fe)-bearing sphalerite. Minerals, 5(2), 117–132.

Craig, J.R. (1973) The Cu–Zn–S system. Mineral Deposita, 8, 81–91.

Danyushevsky, L., Robinson, P., Gilbert, S., Norman, M., Large, R., Mcgoldrick, P., and Shelley, M. (2011) Routine quantitative multi-element analysis of sulphide minerals by laser ablation ICP-MS: Standard development and consideration of matrix effects. Geochemistry Exploration Environment Analysis, 11(1), 51–60.

Danyushevsky, L., Robinson, P., McGoldrick, P., Large, R., and Gilbert, S. (2003) LA-ICPMS of sulphides: evaluation of an XRF glass disc standard for analysis of different sulphide matrixes. Geochimica et Cosmochimica Acta, 67(18), A73.

Frenzel, M., Hirsch, T., and Gutzmer, J. (2016) Gallium, germanium, indium, and other trace and minor elements in sphalerite as a function of deposit type — a meta-analysis. Ore Geology Reviews, 76(9), 52–78.

Gao, H.X., Ren, X.H., Guo, J., Li, F.R., and Li, X. (2011) Geological-geophysical characteristics and orebody prediction of Maozu lead-zinc deposit. Mineral Resources and Geology, 25(2), 152–157 (in Chinese with English abstract).

Garven, G. (1985) The role of regional fluid flow in the genesis of the PinePoint deposit, western Canada sedimentary basin: Economic Geology, 80, 307–324.

Garven, G., and Raffensperger, J.P. (1997) Hydrology and geochemistry of ore genesis in sedimentary basins, in Barnes, H.L., ed., Geochemistry of hydrothermal ore deposits, 3rd ed.: New York, Wiley and Sons, 125–189.

George, L., Cook, N.J., and Ciobanu, C.L. (2016) Partitioning of trace elements in co-crystallized sphalerite–galena–chalcopyrite hydrothermal ores. Ore Geology Reviews, 77, 97–116.

George, L., Cook, N.J., Ciobanu, C.L., and Wade, B.P. (2015) Trace and minor elements in galena: a reconnaissance LA-ICP-MS study. American Mineralogist, 100(2–3), 548–569.

Gregory, D., Meffre, S., and Large, R., (2014) Comparison of metal enrichment in pyrite framboids from a metal-enriched and metal-poor estuary: American Mineralogist, 99, 633–644.

Gregory, D.D., Large, R.R., Halpin, J.A., Baturina, E.L., Lyons, T.W., Wu, S., Danyushevsky, L., Sack, P.J., Chappaz, A., Maslennikov, V.V., and Bull, S.W. (2015) Trace element content of sedimentary pyrite in black shales. Economic Geology, 110, 1389–1410.

Han, R.S., Liu, C.Q., Huang, Z.L., Chen, J., Ma, D.Y., Lei, L., and Ma, G.S. (2007) Geological features and origin of the Huize carbonate-hosted Zn–Pb–(Ag) District, Yunnan, South China. Ore Geology Reviews, 31, 360–383.

He, S.H., Rong, H.H., Shang, W., and Su, J.H. (2006) Geological characteristics and genesis of Maozu lead and zinc deposit, Yunnan. Mineral Resource Geology, 4–5, 397–402 (in Chinese with English abstract).

Höll, R., Kling, M., and Schroll, E. (2007) Metallogenesis of germanium – a review. Ore Geology Reviews, 30, 145–180.

Hu, R.Z., and Zhou, M.F. (2012) Multiple Mesozoic mineralization events in South China – an introduction to the thematic issue. Mineralium Deposita, 47, 579–588.

Huang, Z.L., Chen, J., Han, R.S., Li, W.B., Liu, C.Q., Zhang, Z.L., Ma, D.Y., Gao, D.R., and Yang, H.L. (2004) The Ore Geochemistry and Its Ore Genesis of Huize Super Large Scale Pb-Zn Deposit-Discussion on the Relationship between Pb-Zn Mineralization and Emeishanbasalt. Beijing: Geology Publishing Company Press, 1–187 (in Chinese).

Jeppsson, M.L. (1989) Mineral chemistry of silver in antimony and bismuth rich sulphide ore in Bergslagen, central Sweden. Neues Jahrbuch für Mineralogie Monatshefte, 205–216.

Johan, Z. (1988) Indium and germanium in the structure of sphalerite: an example of coupled substitution with Copper. Mineralogy and Petrology, 39(3–4), 211–229.

Kelley, K. D., Leach, D. L., Johnson, C. A., Clark, J. L., Fayek, M., Slack, J. F., Anderson, V.M., Ayuso, R.A., and Ridley, W. I. (2004). Textural, Compositional, and Sulfur Isotope Variations of Sulfide Minerals in the Red Dog Zn-Pb-Ag Deposits, Brooks Range, Alaska: Implications for Ore Formation. Economic Geology, 99(7), 1509–1532.

Leach, D.L. (1993) Mississippi Valley-type lead-zinc deposits. Geological Association of Canada Special Paper, 40(3), 108–117.

Leach, D.L., and Taylor, R.D. (2009) Mississippi Valley-type lead-zinc deposit model: U.S. Geological Survey Open-File Report, 1213, 5p.

Leach, D.L., Macquar, J.C., Lagneau, V., Leventhal, J., Emsbo, P., and Premo, W. (2006) Precipitation of lead-zinc ores in the Mississippi Valley type deposit at Trèves, Cévennes region of southern

France. Geofluids, 6, 24–44.

Leach, D.L.，Sangster, D.F., Kelley KD，et al. (2005) Sediment-hosted lead-zinc deposits: a global perspective. Economic Geology 100th Anniversary Volume, 100, 561﹣607.

Li, Z.L. (2016) Geological geochemical characteristics and prospecting directions in the Fule lead-zinc deposit, Yunnan Province. Master Degree Thesis. Guiyang: Institute of Geochemistry, Chinese Academy of Sciences, 1–75 (in Chinese with English abstract).

Li, Z.L., Ye, L., Hu, Y.S., and Huang, Z.L. (2018a) Geological significance of nickeliferous minerals in the Fule Pb–Zn deposit, Yunnan Province, China. Acta Geochimica, 37(5), 684–690.

Li, Z.L., Ye, L., Huang, Z.L., Zhou, J.X., Hu, Y.S., and Nian, H.L. (2018b) Mineralogical characteristics and geological significance of Copper minerals in Fule Pb-Zn deposit, Yunnan Province, China. Geological Journal of China Universities, 24(2), 200–209 (in Chinese with English abstract).

Liu, H.C., and Lin, W.D. (1999) Study on the law of Pb–Zn–Ag ore deposit in northeast Yunnan, China. Yunnan University Press, Kunming, 1–468 (in Chinese).

Liu, H.T., and Zhang, Y.X. (2013) Study on leakage anomalies techniques of geochemical prospecting – Giving an example of Maozu Pb-Zn mining district, Qiaojia, Yunnan. Mineral Resources and Geology, 27(5), 403–408 (in Chinese with English abstract).

Liu, W.Z. (2009) Geological and geochemical characteristics and metallogenic mechanism analysis of the Pb–Zn deposit in Maozu, Yunnan, China. Journal of Chengdu University of Technology, 36, 480–486 (in Chinese with English abstract).

Lueth, V.W., Megaw, P.K.M., Pingitore, N.E., and Goodell, P.C. (2000) Systematic Variation in Galena Solid-Solution Compositions at Santa Eulalia, Chihuahua, Mexico. Economic Geology, 95, 1673–1687.

Mladenova, V., and Valchev, S. (1998) Ga/Ge ratio in sphalerite from the carbonate-hosted Sedmochislenitsi Deposit as a temperature indication of initial fluids. Spis. Bulgar. Geol. Druzh., 59(2–3), 49–54.

Mo, X.Y., Chen, T.Y., He, L.T., Jiang, S.D., Zhang, Y.C., and Yang, C. (2013) The Kunyang group in Dongchuan, Yunnan, China. Kunming: Yunnan Science and Technology Press, 1–168 (in Chinese).

Möller, P. (1987) Correlation of homogenization temperatures of accessory minerals from sphalerite-bearing deposits and Ga/Ge model temperatures. Chemical Geology, 61, 153–159.

Moskalyk, R.R. (2003) Gallium: the backbone of the electronics industry. Minerals Engineering, 16, 921–929.

Oftedahl, I. (1940) Untersuchungen über die Nebenbestandteile von Erzmineralien norwegischer zinkblendführender Vorkommen. Skrift. Norsk Vidensk. Akad. Oslo, Math. Naturv. Kl., 8, 1–103.

Renock, D., and Becker, U. (2011) A first principles study of coupled substitution in galena. Ore Geology Reviews, 42, 71–83.

Sangster, D.F. (1996) Mississippi Valley-type lead-zinc, Geology of Canadian Mineral Deposit Types: Geological Survey of Canada. Geology of Canada, (8), 253–261.

Tu, G.C. (1984) Geochemistry of Strata-bound Ore Deposits in China (Volumes I). Science Press, Beijing, 13–69 (in Chinese with English abstract).

Van Hook, H.J. (1960) The ternary system Ag2S-Bi2S3-PbS. Economic Geology, 55, 759–788.

Watling, R.J., Herbert, H.K., Barrow, I.S., and Thomas, A.G. (1995) Analysis of diamonds and indicator minerals for diamond exploration by laser ablation/inductively coupled plasma mass spectrometry. Analyst, 120(5), 1357–1364.

Wei, A., Xue, C., Xiang, K., Li, J., Liao, C., and Akhter, Q.J. (2015) The ore-forming process of the Maoping Pb–Zn deposit, Northeastern Yunnan, China: Constraints from cathodoluminescence (CL) petrography of hydrothermal dolomite. Ore Geology Reviews, 70, 562–577.

Wei, C., Huang, Z.L., Yan, Z.F., Hu, Y.S., Ye, L. (2018a) Trace Element Contents in Sphalerite from the Nayongzhi Zn-Pb Deposit, Northwestern Guizhou, China. Minerals, 8(11): 490-512.

Wei, C., Ye, L., Huang, Z.L., Gao, W., Hu, Y.S., Li, Z.L., Zhang, J.W. (2018b) Ore Genesis and Geodynamic Setting of Laochang Ag-Pb-Zn-Cu Deposit, Southern Sanjiang Tethys Metallogenic Belt, China: Constraints from Whole Rock Geochemistry, Trace Elements in Sphalerite, Zircon U-Pb Dating and Pb Isotopes. Minerals, 8(11): 516-544.

Wei, C., Ye, L., Hu, Y.S., Danyushevskiy, L., Li, Z.L., Huang, Z.L. (2019)A Distribution and occurrence of Ge and related trace elements in sphalerite from the Lehong carbonate-hosted Zn-Pb deposit, northeastern Yunnan, China: Insights from SEM and LA-ICP-MS studies. Ore Geology Reviews doi.org/10.1016/j.oregeorev.2019 .103175

Wu, Y. (2013) The age and ore-forming process of MVT deposits in the boundary area of Sichuan-Yunnan-Guizhou provinces, Southwest China. Doctor Degree Thesis. Beijing: China University of Geosciences, 1–167 (in Chinese with English abstract).

Ye, L., Cook, N.J., Ciobanu, C.L., Liu, Y.P., Zhang, Q., Liu, T.G., Gao, W., Yang, Y.L., and Danyushevskiy, L. (2011) Trace and minor elements in sphalerite from base metal deposits in South China: a LA-ICPMS study. Ore Geology Reviews, 39, 188–217.

Ye, L., Gao, W., Yang, Y.L., Liu, T.G., and Peng, S.S. (2012) Trace elements in sphalerite in Laochang Pb-Zn polymetallic deposit, Lancang, Yunnan Province, Acta Petrologica Sinica, 28(5), 1362–1372 (in Chinese with English abstract).

Ye, L., Li, Z.L., Hu, Y.S., Huang, Z.L., Zhou, J.X., Fan, H.F., and Danyushevsky, L. (2016) Trace elements in sulfide from the Tianbaoshan Pb-Zn deposit, Sichuan Province, China: A LA-ICPMS study. Acta Petrologica Sinica, 32(11), 3377–3393 (in Chinese with English abstract).

Yuan, B., Zhang, C.Q., Yu, H.J., Yang, Y.M., Zhao, Y.X., Zhu, C.C., Ding, Q.F., Zhou, Y.B., Yang, J.C., and Xu, Y. (2018) Element enrichment characteristics: insights from element geochemistry of sphalerite in Daliangzi Pb–Zn deposit, Sichuan, Southwest China. Journal of Geochemical Exploration, 186, 187–201.

Zhang, C.Q., Wu, Y., Hou, L., and Mao, J.W. (2015) Geodynamic setting of mineralization of Mississippi Valley-type deposits in world-class Sichuan-Yunnan-Guizhou Zn-Pb triangle, southwest China: Implications from age-dating studies in the past decade and the Sm-Nd age of Jinshachang deposit. Journal of Asian Earth Sciences, 103, 103–114.

Zhang, K., and Li, H.Y. (2014) Migration of trace elements in pyrite from orogenic gold deposits: Evidence from LA-ICP-MS analyses. Acta Geologica Sinica (English Edition), 88 (Suppl. 2), 841–842.

Zhang, Q. (1987) Trace elements in galena and sphalerite and their geochemical significance in distinguishing the genetic types of Pb–Zn ore deposits. Chinese Journal of Geochemistry, 6, 177–190.

Zhang, R.W. (2013) Geochemical characteristics and genetic type of the Maozu Pb-Zn deposit in Yunnan province, China. Kunming: Kunming University of Science and Technology, 1–82 (in Chinese with English abstract).

Zhang, W.J. (1984) The sedimentary genesis and metallogenic rules of Pb-Zn deposits in northeast

Yunnan province. Geology and exploration, (7), 11–16 (in Chinese).

Zhang, Z.B., Li, C.Y., Tu, G.C., Xia, B., and Wei, Z.Q. (2006) Geotectonic evolution background and ore-forming process of Pb-Zn deposits in Chuan-Dian-Qian area of Southwest China. Geotectonica et Metallogenia, 30(3), 343–354 (in Chinese with English abstract).

Zhou, J.X., Huang, Z.L., and Yan, Z.F. (2013) The origin of the Maozu carbonate-hosted Pb–Zn deposit, southwest China: Constrained by C–O–S–Pb isotopic compositions and Sm-Nd isotopic age: Journal of Asian Earth Sciences, 73, 39–47.

Zhou, J.X., Xiang, Z.Z., Zhou, M.F., Feng, Y.X., Luo, K., Huang, Z.L., and Wu. T. (2018) The giant Upper Yangtze Pb-Zn province in SW China: Reviews, new advances and a new genetic model. Journal of Asian Earth Sciences, 154, 280-315.

Zhu, C.W., Wen, H.J., Zhang, Y.X., Fu, S.H., Fan, H.F., and Cloquet, C. (2017) Cadmium isotope fractionation in the Fule Mississippi Valley-type deposit, Southwest China. Mineralium Deposita, 52, 675–686.

Figure captions

Figure 1. Regional tectonic sketch map of southern China and the location of the Sichuan-Yunnan-Guizhou Pb-Zn metallogenic province (SYGMP) (modified from Huang et al. 2004; Zhou et al. 2018). (Color online.)

Figure 2. Generalized stratigraphic column of the Maozu Pb-Zn deposit (modified from Zhou et al. 2018) (Color online.)

Figure 3. (**a**) Geological map of the Maozu Pb-Zn deposit (modified after Liu 2009). (**b**) Representative cross-section A-A* through the deposit. (Color online.)

Figure 4. Outcrop photographs coupled with photomicrographs of thin sections from lower layer (LL), vein layer (VL) and upper layer (UL) three ore bodies in the Maozu deposit. (**a**) UL occurs as stratiform in dolostone below the phosphorus-bearing layer. (**b)** Gangue minerals in the UL are dominated by fluorite and dolomite. (**c)** Sphalerite is cross-cut by a later galena vein. (**d)** Galena edges are replaced by later tetrahedrite. (**e**) VL ore bodies occur as veinlets in the tectonic fractures. (**f**) Pb-Zn ores coexist with calcite. (**g**) Fluorite is cut by sphalerite and galena veins. (**h**) Galena is wrapped with coarse pyrite (Py2). (**i**) LL occurs in siliceous dolomite as in stratoid form. (**j**) Quartz is the dominant gangue mineral in the LL. (**k**) Fine pyrite (Py1) in sphalerite formed earlier than sphalerite. (**l**) Minor bitumen occurs around the sulfides. Abbreviations: Sp=Sphalerite; Gn=Galena; Py=Pyrite; Tet=Tetrahedrite; Flu=Fluorite; Q=Quartz; Cal=Calcite; Dol=Dolomite and Bit=Bitumen; UL=Upper layer; VL=Vein layer; and LL=Lower layer. (Color online.)

Figure 5. Mineral paragenesis in the Maozu Pb-Zn deposit. (Color online.)

Figure 6. Trace element concentrations (LA-ICP-MS) in sphalerite from the Maozu Pb-Zn deposit and trace element concentrations in different genesis deposits (the data on the skarn, SEDEX, VMS, MVT, and Huize are from Ye et al. 2011; data on Tianbaoshan are from Ye et al. 2016; data on Daliangzi are from Yuan et al. 2018, and data on Fule are from Li 2016). (Color online.)

Figure 7. Correlation plots of sphalerite: (**a**) Fe *vs* Cd, (**b**) Mn *vs* Cd, (**c**) Fe *vs* Mn, (**d**) Co *vs* Ni, (**e**) Cu *vs* Ge, (**f**) Cu *vs* Ag, (**g**) Ge *vs* Ag, (**h**) Sb *vs* Ge, (**i**) Mx *vs* My, (**j**) In *vs* Sn, (**k**) (Cu + Sb) *vs* (Ag + Ge), (**l**) Cu *vs* Sb, (**m**) Sb *vs* Ag. Galena of (**n**) Ag *vs* Sb, and (**o**) (Bi + Sb) *vs* (Cu + Ag + Tl). Note: r=correlation coefficient; k=slope; dashed lines=regression lines; solid lines=lines with different WRs. (Color online.)

Figure 8. Histogram of trace elements for galena of the Maozu Pb-Zn deposit. (Color online.)

Figure 9. Representative time-resolved depth acquisition profiles for sphalerite (**a-d**) and galena (**e-f**) analyzed by LA-ICP-MS. (Color online.)

Figure 10. Mapping images of sphalerite in the Maozu Pb-Zn deposit. (**a**) Scanning area of sphalerite. (Color online.)

Figure 11. Binary plots of (**a**) Fe *vs* Mn, (**b**) Fe *vs* Bi, (**c**) Mn *vs* Bi and (**d**) Ag *vs* Bi in galena from Maozu and other genesis Pb-Zn deposits (the data of SEDEX are from Ye et al. 2011; George et al. 2015, 2016; the MVT data are from Ye et al. 2016). (Color online.)

Figure 12. Binary plots of (**a**) Mn *vs* Fe, (**b**) Mn *vs* Co, (**c**) Mn *vs* Ge and (**d**) Cd/Fe *vs* Mn in sphalerite from Maozu and other genesis Pb-Zn deposits (the data of other genesis deposits are from Cook et al. 2009; Ye et al. 2011, 2016; Li 2016; Yuan et al. 2018; Wei et al., 2018a, b). (Color online.)

Table captions

Table 1 Trace elements in sphalerite and galena from the Maozu Pb-Zn deposit, Yunnan, China (ppm)

Note: Sp=Sphalerite; Gn=Galena; S.D.=Standard deviation; UL=Upper layer; VL=Vein layer; LL=Lower layer; “-”=Not detected or below the detectable limit.

Table 2 Concentrate variations for trace elements of sphalerite in Pb-Zn deposits of different genetic types analyzed by LA-ICP-MS (ppm)

Table 1 Trace elements in sphalerite and galena from the Maozu Pb-Zn deposit, Yunnan, China (ppm)

Mineral	Layer		Mn	Fe	Co	Ni	Cu	Ge	As	Se	Ag	Cd	In	Sn	Sb	Pb	Bi
Sp	UL	Mean	76.1	10257	3.01	-	786	138	19.6	-	87.6	2926	0.62	0.58	294	43.9	-
MZ-8		Median	73.7	9833	1.77	-	311	113	7.01	-	35.7	2963	0.13	0.24	95.6	30.0	-
(N=8)		MAD	17.3	439	1.22	-	177	73.3	3.70	-	21.9	43.2	0.32	0.14	76.2	21.6	-
		Min	51.5	9316	0.45	-	33.5	6.81	1.27	-	4.46	2787	0.01	0.08	0.49	1.02	-
		Max	97.9	13057	12.2	0.08	2074	342	77.9	1.86	254	3019	2.75	1.98	835	135	0.02
Sp	UL	Mean	136	4115	5.07	-	318.18	62.0	6.88	-	14.4	3618	0.54	0.36	32.2	24.0	-
MZ-30		Median	141	4199	4.88	-	333	42.1	4.28	-	12.8	3773	0.33	0.32	13.2	14.4	-
(N=8)		MAD	19.9	106	2.12	-	195	32.9	3.33	-	7.22	710	0.22	0.15	10.1	10.9	-
		Min	2.78	2915	2.65	-	43.1	3.95	0.82	-	6.05	2459	0.05	0.05	4.98	2.74	-
		MAX	206	4884	7.54	0.06	897	185	26.8	2.31	28.2	4569	1.86	1.34	120	64.4	0.01
Sp	UL	Mean	114	11114	17.2	0.73	684	83.0	6.32	-	10.6	2723	14.9	14.6	116	5.81	-
MZ-51		Median	120	11738	17.3	0.75	244	64.4	2.94	-	5.02	2724	7.54	9.31	21.9	2.11	-
(N=8)		MAD	28.6	2941	10.1	0.19	191	62.0	1.91	-	1.68	341	6.11	7.38	14.7	1.46	
		Min	54.0	6073	4.49	0.42	32.6	0.32	1.03	-	3.50	2237	0.15	0.50	0.35	0.62	-
		MAX	154	14752	28.2	0.94	1999	227	16.0	3.39	45.9	3236	72.5	47.5	633	30.7	0.01
Sp	UL	Mean	61.0	9917	18.7	1.49	362	65.9	15.5	-	4.11	3438	7.00	32.0	30.3	8.56	-
MZ-67		Median	57.5	9848	18.7	1.28	201	25.9	3.04	-	6.11	3563	0.44	0.40	26.2	1.37	-
(N=8)		MAD	27.2	554	1.84	0.21	37.0	17.4	2.29	-	4.29	137	0.42	0.31	24.7	1.37	-
		Min	25.2	8621	14.2	0.94	46.8	4.03	0.75	-	1.44	2746	0.02	0.12	1.31	2.74	-
		MAX	96.3	11021	26.0	3.08	1007	186	56.3	-	11.6	3778	32.6	179	134	13.7	0.01
Gn	UL	Mean	-	-	-	-	0.28	-	-	0.47	561	32.9	-	2.32	724	-	0.16
MZ-67		Median	-	-	-	-	0.22	-	-	0.47	575	33.9	-	2.33	740	-	0.16

(N=6)		MAD	-	-	-	-	0.06	-	-	-	20.4	3.74	-	0.32	31.9		0.02
		Min	-	-	0.01	0.14	0.15	-	-	0.44	506	24.7	-	1.89	654	-	0.14
		MAX	-	-	-	-	0.66	-	-	0.50	606	37.6	-	2.78	773	-	0.19
Sp	UL	Mean	75.7	4225	7.27	-	609	75.1	66.6	-	89.3	3454	96.2	18.5	180	228	-
MZ-69		Median	75.9	3509	5.95	-	574	55.7	62.9	-	89.8	3506	29.8	30.2	121	219	-
(N=8)		MAD	14.9	1672	3.36	-	55.6	14.7	19.8	-	31.9	210	21.3	22.7	46.8	85.1	-
		Min	41.9	698	2.21	-	308	20.8	36.0	-	40.4	3185	3.06	6.72	29.0	90.4	-
		MAX	109	13025	14.4	0.19	1193	143	123	3.40	149	3731	397	32.8	776	399	0.01
Sp	VL	Mean	31.2	5554	1.62	-	274	60.0	70.4	-	7.47	4122	5.15	3.86	19.2	11.3	-
MZ-12		Median	29.7	5312	1.55	-	106	50.8	0.91	-	6.01	4037	0.07	0.44	3.79	6.17	-
(N=8)		MAD	12.8	572	0.71	-	73.4	37.4	1.98	-	2.17	100	0.07	0.31	1.50	2.05	-
		Min	15.4	4386	0.33	-	9.23	0.75	1.03	-	2.54	3739	0.00	0.10	0.75	1.37	-
		MAX	53.5	7358	3.70	-	1037	196	275	-	15.1	4685	20.6	12.3	78.3	50.7	0.01
Gn	VL	Mean	-	-	-	-	0.95	-	-	68.1	619	33.8	-	8.03	705	-	0.81
MZ-12		Median	-	-	-	-	0.74	-	-	72.1	640	29.8	-	7.17	724	-	0.60
(N=8)		MAD	-	-	-	-	0.43	-	-	7.99	37.4	7.60	-	2.85	53.3	-	0.12
		Min	-	6.63	0.01	0.03	0.23	-	0.69	13.7	485	21.2	-	3.45	583	-	0.17
		MAX	-	-	-	-	2.56	-	-	96.4	703	56.7	-	16.6	795	-	1.90
Sp	VL	Mean	61.7	17832	22.5	-	989	7.29	11.7	-	31.6	3161	483	496	87.7	20.8	-
MZ-14		Median	65.3	19298	22.6	-	659	2.01	1.04	-	13.5	3177	532	393	10.8	3.43	-
(N=8)		MAD	11.3	1073	3.81	-	255	1.17	11.3	-	11.8	97.9	286	273	10.7	3.43	-
		Min	32.7	11697	8.77	-	109	0.66	1.36	-	1.34	2386	35.7	15.8	2.05	1.37	-
		MAX	79.9	20570	35.1	0.67	2752	34.7	20.9	3.14	141	3618	1191	2192	486	57.5	-
Gn	VL	Mean	-	-	-	-	0.37	-	-	4.07	869	32.8	-	4.36	990	-	0.22
MZ-14		Median	-	-	-	-	0.37	-	-	3.57	863	36.4	-	4.52	988	-	0.19
(N=5)		MAD	-	-	-	-	0.09	-	-	1.72	21.1	4.33	-	0.48	15.62	-	0.09

		Min	-	6.31	-	-	0.27	-	-	1.26	832	19.7	-	2.70	961	-	0.10
		MAX	-	-	-	-	0.47	-	0.47	6.96	910	40.7	-	5.29	1033	-	0.42
Sp	LL	Mean	38.4	4069	2.34	-	411	89.6	76.2	-	14.2	3760	93.0	0.96	48.3	6.43	-
MZ-2		Median	24.3	2845	1.55	-	743	40.8	38.4	-	16.2	3485	0.02	0.18	97.1	5.35	-
(N=8)		MAD	14.0	887	1.23	-	432	40.4	25.7	-	4.10	374	0.50	0.07	91.6	1.55	-
		Min	10.1	1555	0.04	-	20.7	0.30	23.5	-	6.92	3082	0.01	0.06	0.81	1.08	-
		MAX	87.1	8156	8.62	0.13	1029	238	164	1.73	29.1	4644	464	6.39	123	15.2	-
Sp	LL	Mean	101	2051	0.62	-	322	65.1	35.5	-	18.6	4052	7.94	3.32	63.2	46.6	-
MZ-35		Median	98.4	2033	0.44	-	235	39.2	10.3	-	14.1	4087	3.31	1.59	33.6	37.7	-
(N=8)		MAD	11.5	142	0.21	-	157	31.2	2.88	-	4.80	225	2.91	1.45	8.42	10.9	-
		Min	50.0	1830	0.10	-	31.3	2.49	0.92	-	5.93	3479	0.11	0.17	9.92	26.0	-
		MAX	141	2327	1.54	-	994	201	117	3.52	41.4	4519	40.7	14.5	177	82.2	0.04
Gn	LL	Mean	-	-	-	-	2.02	-	-	55.9	398	40.2	-	0.75	460	-	5.13
MZ-35		Median	-	-	-	-	1.94	-	-	59.3	426	39.0	-	0.76	498	-	3.32
(N=7)		MAD	-	-	-	-	0.61	-	-	9.28	37.9	4.45	-	0.11	37.1	-	1.25
		Min	-	-	-	0.02	1.25	-	-	37.8	293	31.6	-	0.61	342	-	1.56
		MAX	-	-	-	-	3.04	-	-	68.7	464	51.6	-	0.89	535	-	14.2

Note: Sp- Sphalerite; Gn- Galena; MAD- Median absolute deviation; UL- Upper layer; VL- Vein layer; LL- Lower layer; “-“- Not detect or below detectable limit.

Table 2 Concentrate variations for trace elements of sphalerite in different genetic types Pb-Zn deposits analyzed by LA-ICPMS (ppm)

Ore deposit/ genetic type		Mn	Fe	Co	Ni	Cu	Ge	As	Se	Ag	Cd	In	Sn	Sb	Te	Tl	Pb	Refernence
The target deposit																		
Maozu (*N=72*)	Mean	77.4	7681	8.81	0.74	514	71.8	32.3	2.58	31.5	3473	81.4	73.9	96.3	0.35	0.09	42.6	this paper
	Median	74.5	6273	4.59	0.67	334	37.0	9.36	2.48	12.5	3465	2.84	1.52	36.3	0.32	0.07	8.22	
	Min	2.78	698	0.04	0.04	11.6	0.30	0.75	1.73	1.60	2237	0.004	0.08	0.07	0.15	0.004	0.001	
	Max	206	20570	35.1	3.08	2394	342	275	3.52	257	4685	1191	1814	865	0.60	0.43	399	
SYGMP-MVT deposits																		
Fule (*N=88*)	Mean	2.82	2636	13.5	2.06	1004	170	191	-	11. 6	17182	-	-	248	-	-	198	unpublished
	Median	3.25	2543	14.2	2.21	1035	184	153	-	32.3	3221	-	-	458	-	-	254	
	Min	0.98	1305	8.08	0.59	5.09	0.54	1.59	-	1.55	2833	-	-	0.18	-	-	0.2	
	Max	10.6	5370	19.7	5.03	5650	632	1534	69.2	91.4	46662	3.25	31.71	2317	0.82	1.09	1182	
Daliangzi (*N=85*)	Mean	7.40	13713	3.79	1.99	1485	66.9	109	-	225	5289	1.41	2.52	242	-	0.57	680	Yuan et al., 2018
	Median	5.13	11250	3.12	1.27	314	26.8	20.5	-	31.6	3681	0.11	0.74	66.1	-	0.13	52.9	
	Min	0.11	570	0.44	0.29	8.79	0.11	0.27	-	1.85	529	0.002	0.24	0.13	-	0.001	1.08	
	Max	48.9	57683	10.3	10.8	15113	328	1863	-	4037	19479	15.3	24.7	3073	-	10.9	31653	
Tianbaoshan (*N=57*)	Mean	10.1	16309	44.2	3.11	2903	29.5	276	2.42	205	7245	1.25	3.27	202	0.47	0.06	166	Ye et al., 2016
	Median	10.5	16219	11.1	0.09	391	11.8	13.8	0.79	98.5	4761	0.01	0.38	35.0	0.48	0.01	59.9	
	Min	1.92	7251	3.03	0.03	40.6	0.52	0.56	0.48	25.4	2915	0.001	0.03	0.68	0.15	0.004	1.18	
	Max	20.1	30675	855	155	20042	206	4748	40.3	1011	28278	10.2	76.0	1546	0.89	0.67	3821	
Huize	Mean	96.5	21193	0.03	0.07	285	81.9	33.9	0.62	22.8	2131	0.72	1.68	28.5	0.12	0.08	9.99	Ye et al.,

(*N=24*)	Median	92.5	18840	0.02	0.03	186	59.5	1.62	0.71	16.4	1730	0.06	0.25	2.52	0.05	0.02	4.75	2011
	Min	7.27	5063	0.001	0.01	7.11	3.05	0.14	0.12	6.10	929	0.001	0.07	0.001	0.01	0.001	0.40	
	Max	305	45776	0.06	0.24	1169	348	399	1.65	74.4	4502	5.81	27.6	297	0.36	0.85	69.1	
MVT deposit (Mexico)																		
	Mean	27.6	61805	0.34	0.68	20.2	704	510	1.94	3.52	5109	0.20	3.20	33.9	0.23	113	2094	
Tres Marias	Median	38.8	74829	0.39	0.23	13.4	970	532	2.00	2.69	5150	0.17	2.20	15.5	0.24	141	1376	Cook et al.,
(*N=23*)	Min	4.40	16681	0.09	0.12	1.00	174	122	1.23	1.64	3354	0.04	0.29	0.71	0.18	29.5	374	2009
	Max	50.0	106107	0.48	2.33	80.6	1242	1321	3.08	6.60	6581	0.70	11.1	161	0.27	179	12496	
VMS deposit																		
	Mean	531	1937	0.03	0.31	382	10.2	-	1.09	5.72	4745	0.05	0.10	3.25	0.29	0.24	462	Cook et al.,
Vorta DMV	Median	571	2084	0.02	0.31	381	8.90	-	1.05	3.12	4771	0.05	0.08	1.24	0.29	0.01	5.64	2009 and
(*N=8*)	Min	165	917	0.02	0.23	131	2.73	-	0.82	1.38	4169	0.04	0.05	0.04	0.21	0.01	0.46	references
	Max	761	2617	0.06	0.39	719	23.4	-	1.40	21.2	5088	0.06	0.24	17.1	0.36	1.14	3426	therein
Eskay	Mean	3265	4882	0.10	1.93	770	2.08	211	2.35	535	3852	1.41	12.6	20420	0.63	3.97	11521	Cook et al.,
Creek	Median	3373	4549	0.09	1.24	402	1.01	48.9	1.70	102	3898	0.20	7.60	4831	0.50	1.10	5390	2009 and
(*N=12*)	Min	2296	3880	0.04	0.47	67.0	0.47	1.00	1.30	6.80	2720	0.10	2.60	5.06	0.18	0.08	1.15	references
	Max	4744	7112	0.17	4.01	3483	13.7	1550	4.10	2785	4955	13.7	31.1	117467	1.40	20.6	50955	therein
	Mean	970	78561	27.8	-	29.4	1.03	-	94.1	3.80	2202	29.7	0.65	0.03	-	-	-	Cook et al.,
Sauda	Median	924	74359	26.0	-	25.5	1.02	-	93.5	3.68	2079	28.0	0.50	0.02	-	-	-	2009 and
(*N=10*)	Min	874	69576	25.0	-	22.0	0.86	-	89.0	2.44	1973	27.0	0.27	0.01	-	-	-	references
	Max	1449	120205	44.0	-	44.0	1.43	-	109	5.48	3488	42.0	1.26	0.10	-	-	-	therein
Zinkgruvan	Mean	513	32337	160	0.74	3.44	1.06	-	1.90	6.51	3812	0.29	0.15	1.23	0.16	-	43.0	Cook et al.,
(*N=5*)	Median	507	31930	15	0.67	3.10	1.07	-	1.90	4.65	3807	0.30	0.11	0.28	0.16	-	2.95	2009 and

	Min	499	31735	157	0.56	1.90	0.82	-	1.90	4.55	3661	0.26	0.08	0.12	0.15	-	1.38	references
	Max	532	33261	164	0.95	5.10	1.19	-	1.90	12.6	3943	0.32	0.25	4.12	0.17	-	193	therein
	Mean	30101	96962	11.4	1.15	1077	2.08	0.52	1.97	5.22	1669	4.59	0.64	0.16	-	0.09	2620	Cook et al.,
Kaveltorp	Median	29491	85634	11.4	0.99	299	1.95	0.52	1.82	5.42	1688	4.55	0.94	0.17	-	0.08	14.3	2009 and
(*N=8*)	Min	27739	79809	10.7	0.69	13.5	1.82	0.52	1.34	3.11	1585	4.05	0.07	0.04	-	0.01	5.93	references
	Max	34816	163123	12.0	1.78	3743	3.09	0.52	2.68	7.57	1731	5.32	1.03	0.35	0.21	0.18	10443	therein
	Mean	4105	96877	170	0.74	4021	3.48	-	32.9	13.7	3251	26.4	0.27	0.06	0.18	0.18	11.8	Cook et al.,
Marketorp	Median	1853	91503	169	0.74	2807	2.08	-	33.2	10.3	3257	26.6	0.15	0.07	0.18	0.06	9.33	2009 and
(*N=8*)	Min	1684	86959	160	0.74	1414	1.78	-	29.1	7.42	2968	24.7	0.09	0.04	0.15	0.02	0.81	references
	Max	18729	119418	188	0.74	14368	12.6	-	35.6	33.6	3619	27.9	0.81	0.08	0.21	0.30	29.1	therein
	Mean	2841	121474	0.84	0.17	248	3.86	2.44	1.69	6.32	8119	186	6.49	0.94	0.20	0.35	23.7	
Laochang	Median	2905	119716	0.53	0.13	176	3.33	0.83	1.44	5.89	8071	179	4.73	0.42	0.24	0.11	2.02	Ye et al.,
(*N=30*)	Min	2438	114390	0.07	0.02	111	1.95	0.14	0.25	4.47	7605	62.0	2.06	0.001	0.03	0.001	0.28	2011
	Max	3711	139194	4.14	1.55	1883	14.1	32.9	3.70	9.49	8947	522	34.9	3.81	0.45	2.40	517	
SEDEX deposit																		
	Mean	2021	109851	2.01	0.08	741	3.07	0.59	0.84	32.9	5291	213	11.3	3.84	0.16	0.02	25.9	
Dabaoshan	Median	2094	110318	0.86	0.05	219	3.09	0.18	0.61	21.7	5359	242	6.32	1.24	0.06	0.01	2.38	Ye et al.,
(*N=26*)	Min	650	99050	0.02	0.01	105	2.44	0.08	0.17	8.71	4364	105	1.33	0.09	0.03	0.001	0.47	2011
	Max	2463	116763	6.16	0.34	5499	3.92	3.00	3.85	186	5609	388	44.5	17.9	0.35	0.13	465	
Skarn deposit																		
Late	Mean	3919	90412	34.3	0.64	251	1.09	-	75.9	1.77	2898	55.5	0.40	0.10	0.36	-	0.52	Cook et al., 2009
Cretaceous	Median	4134	91531	34.4	0.62	168	1.10	-	75.0	1.75	2859	48.6	0.16	0.05	0.31	-	0.43	
(SE Europe)	Min	2545	85805	31.9	0.37	69.0	1.00	-	72.4	1.50	2773	38.6	0.07	0.02	0.29	-	0.12	

(*N=8*)	Max	4476	92590	36.3	1.06	541	1.20	-	81.5	2.06	3256	98.9	1.52	0.32	0.44	0.02	1.20	
Ocna de Fier (*N=37*)	Mean	5308	30549	580	1.22	828	1.07	2.93	6.51	18.9	5865	20.7	0.44	0.59	2.01	0.17	4413	Cook et al., 2009
	Median	3070	20797	278	0.97	112	1.02	0.80	4.55	2.67	5896	10.10	0.13	0.26	0.38	0.10	225	
	Min	905	1619	5.90	0.11	4.60	0.58	0.50	1.50	1.50	4825	0.03	0.05	0.01	0.04	0.02	0.30	
	Max	36136	99262	2828	3.95	13397	1.76	9.60	47.2	356	7146	175	4.83	3.04	12.7	0.91	57625	
Baita Bihor (*N=36*)	Mean	3019	13062	578	8.08	2872	0.95	0.55	7.59	11.6	6923	203	5.15	0.43	1.08	0.05	120	Cook et al., 2009
	Median	3422	11651	567	8.60	162	0.87	0.52	5.45	1.84	7363	49.8	0.40	0.10	0.29	0.04	0.92	
	Min	841	919	2.40	0.24	9.00	0.69	0.34	1.30	1.30	5102	10.3	0.05	0.02	0.16	0.01	0.07	
	Max	4924	32653	1458	17.4	25535	1.51	0.82	30.8	121	7999	867	46.0	2.22	2.95	0.11	3476	
Baisoara (*N=20*)	Mean	446	8216	11.1	0.79	1380	7.17	143	5.72	74.9	43576	12.9	30.4	154	0.83	25.0	2089	Cook et al., 2009
	Median	24.4	1185	9.95	0.70	1394	1.15	51.9	3.10	49.0	28717	2.30	11.7	30.0	0.72	17.0	541	
	Min	0.43	118	2.00	0.07	6.00	0.58	14.9	1.10	3.00	423	0.03	0.92	17.5	0.27	8.10	215	
	Max	5263	30578	23.5	2.41	6879	47.9	474	19.3	311	132317	74.8	121	1245	1.60	72.0	12140	
Lefevre (CLY) L-12 (*N=8*)	Mean	3050	103995	328	4.59	306	2.25	0.90	16.2	3.38	10804	179	0.12	0.15	0.33	0.14	3.83	Cook et al., 2009
	Median	2789	102017	331	0.53	142	2.09	0.90	16.5	3.09	10602	183	0.11	0.09	0.33	0.09	2.37	
	Min	2396	92428	300	0.25	107	1.73	0.90	12.9	1.95	10071	139	0.06	0.03	0.33	0.03	0.70	
	Max	5186	119230	355	19.2	1268	3.58	0.90	19.2	5.19	11945	203	0.20	0.41	0.33	0.44	8.65	
Konnerudkollen Ko99.2 (*N=5*)	Mean	545	4236	1547	5.10	389	0.75	0.48	24.2	93.2	2449	7.58	0.09	0.08	12.2	-	3451	Cook et al., 2009
	Median	551	4332	1542	4.55	350	0.79	0.50	12.30	4.79	2469	7.70	0.07	0.08	12.2	-	17.2	
	Min	483	3981	1526	2.13	103	0.59	0.37	10.5	3.05	2321	6.50	0.05	0.04	12.2	-	9.70	
	Max	609	4405	1585	11.9	633	0.83	0.57	72.0	446	2495	8.20	0.15	0.11	12.2	1.55	17158	

Kamioka **Kam-1** **(*N=8*)**	Mean	1380	20413	231	3.21	3.21	0.83	-	60.9	14.0	5446	0.99	0.20	0.06	1.92	0.24	1345	Cook et al., 2009
	Median	1397	20483	231	3.13	3.20	0.85	-	41.0	2.25	5455	0.98	0.16	0.04	1.90	0.17	30.3	
	Min	1249	19408	222	3.03	2.20	0.70	-	21.4	1.70	5334	0.76	0.09	0.02	0.35	0.09	0.22	
	Max	1460	21553	245	3.54	4.20	0.87	-	190	94.4	5521	1.37	0.38	0.13	3.52	0.46	10630	
Skarn (China)																		
Hetaoping **(*N=24*)**	Mean	2985	51001	212	0.10	583	2.79	0.28	31.3	8.08	4643	0.05	0.10	4.43	0.12	0.01	37.2	Ye et al., 2011
	Median	2817	37964	110	0.04	10.3	2.78	0.16	23.6	6.07	4254	0.01	0.10	2.81	0.05	0.001	6.32	
	Min	1254	20530	65.9	0.01	6.06	2.53	0.09	7.08	4.43	4033	0.001	0.06	0.001	0.02	0.001	0.20	
	Max	5486	105927	478	0.47	7714	3.13	1.76	86.7	23.3	6472	0.17	0.12	19.9	0.35	0.07	368	
Luziyuan **(*N=39*)**	Mean	3466	46233	347	5.87	649	2.03	52.9	43.8	5.26	1808	0.09	0.78	22.7	0.14	0.05	1697	Ye et al., 2011
	Median	1237	44529	377	0.47	44.5	2.70	0.88	1.54	4.49	1923	0.04	0.15	4.12	0.04	0.02	29.5	
	Min	442	-	63.4	0.08	4.99	0.12	0.08	-	0.42	1199	0.005	0.001	0.005	-	-	-	
	Max	22642	99651	1267	51.1	6636	3.51	324	327	22.4	2387	0.82	8.74	383	0.70	0.32	48958	

Note: “-“- Not detect or below detectable limit.

Fig.1

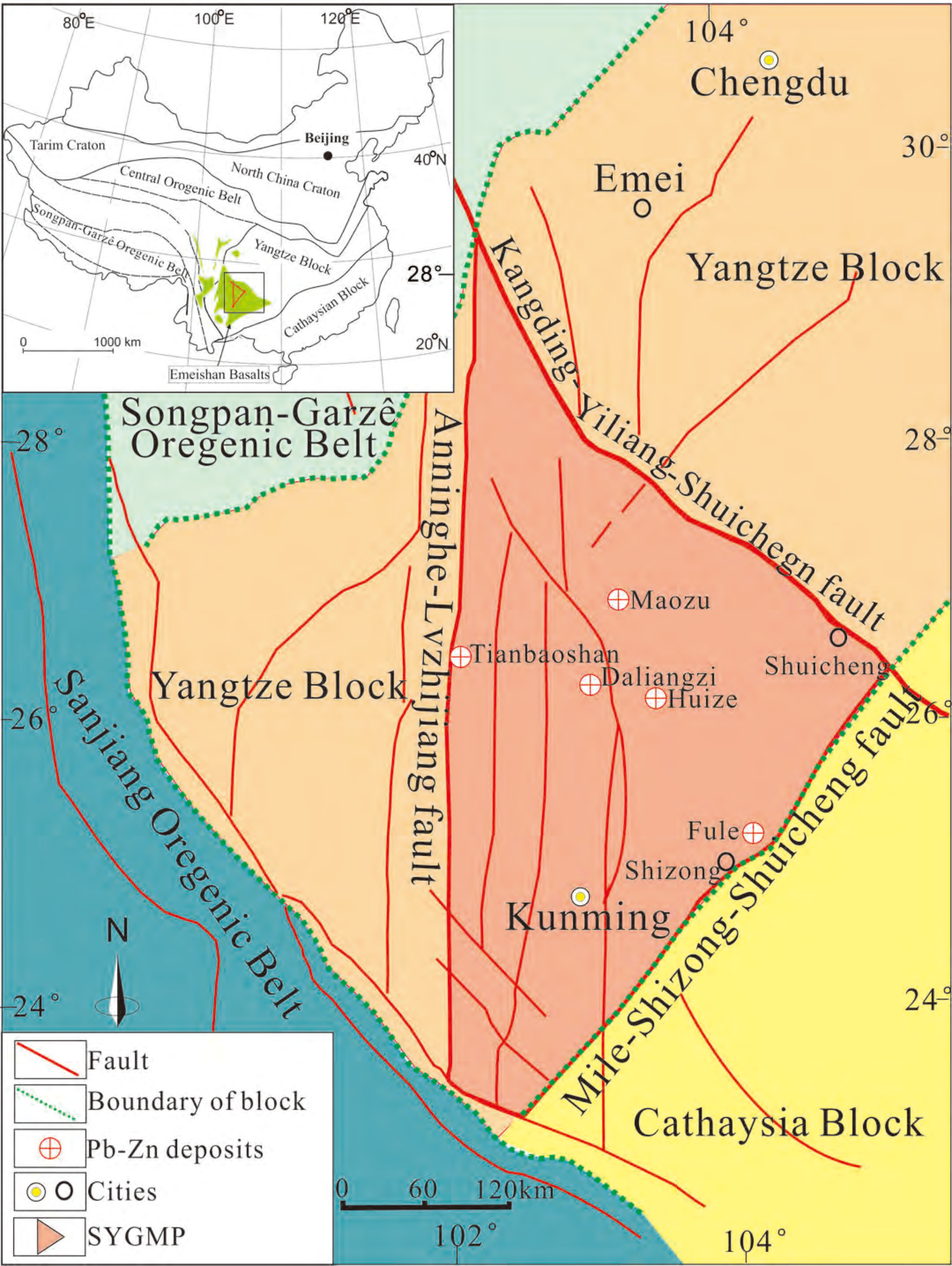
80°E
100°E
120°E
Tarim Craton
Beijing
40°N
Central Orogenic Belt
North China Craton
Songpan-Garzê Oregenic Belt
Yangtze Block
28°
Cathaysian Block
0
1000 km
20°N
Emeishan Basalts
104°
Chengdu
30°
Emei
Yangtze Block
Kangding-Yiliang-Shuichegn fault
Songpan-Garzê Oregenic Belt
28°
Anninghe-Lvzhijiang fault
Maozu
Tianbaoshan
Dalianzi
Huize
Shuicheng
Yangtze Block
26°
Sanjiang Oregenic Belt
Mile-Shizong-Shuicheng fault
Fule
Shizong
Kunming
N
24°
Cathaysia Block
Fault
Boundary of block
Pb-Zn deposits
Cities
SYGMP
0
60
120km
102°
104°

Fig.2

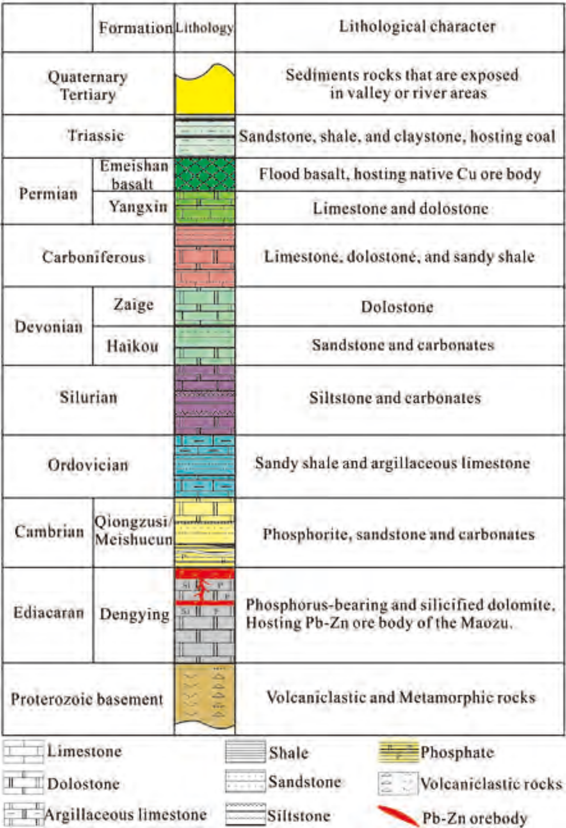

	Formation	Lithology	Lithological character
Quaternary Tertiary			Sediments rocks that are exposed in valley or river areas
Triassic			Sandstone, shale, and claystone, hosting coal
Permian	Emeishan basalt		Flood basalt, hosting native Cu ore body
	Yangxin		Limestone and dolostone
Carboniferous			Limestone, dolostone, and sandy shale
Devonian	Zaige		Dolostone
	Haikou		Sandstone and carbonates
Silurian			Siltstone and carbonates
Ordovician			Sandy shale and argillaceous limestone
Cambrian	Qiongzusi/ Meishucun		Phosphorite, sandstone and carbonates
Ediacaran	Dengying		Phosphorus-bearing and silicified dolomite, Hosting Pb-Zn ore body of the Maozu.
Proterozoic basement			Volcaniclastic and Metamorphic rocks

Fig.3

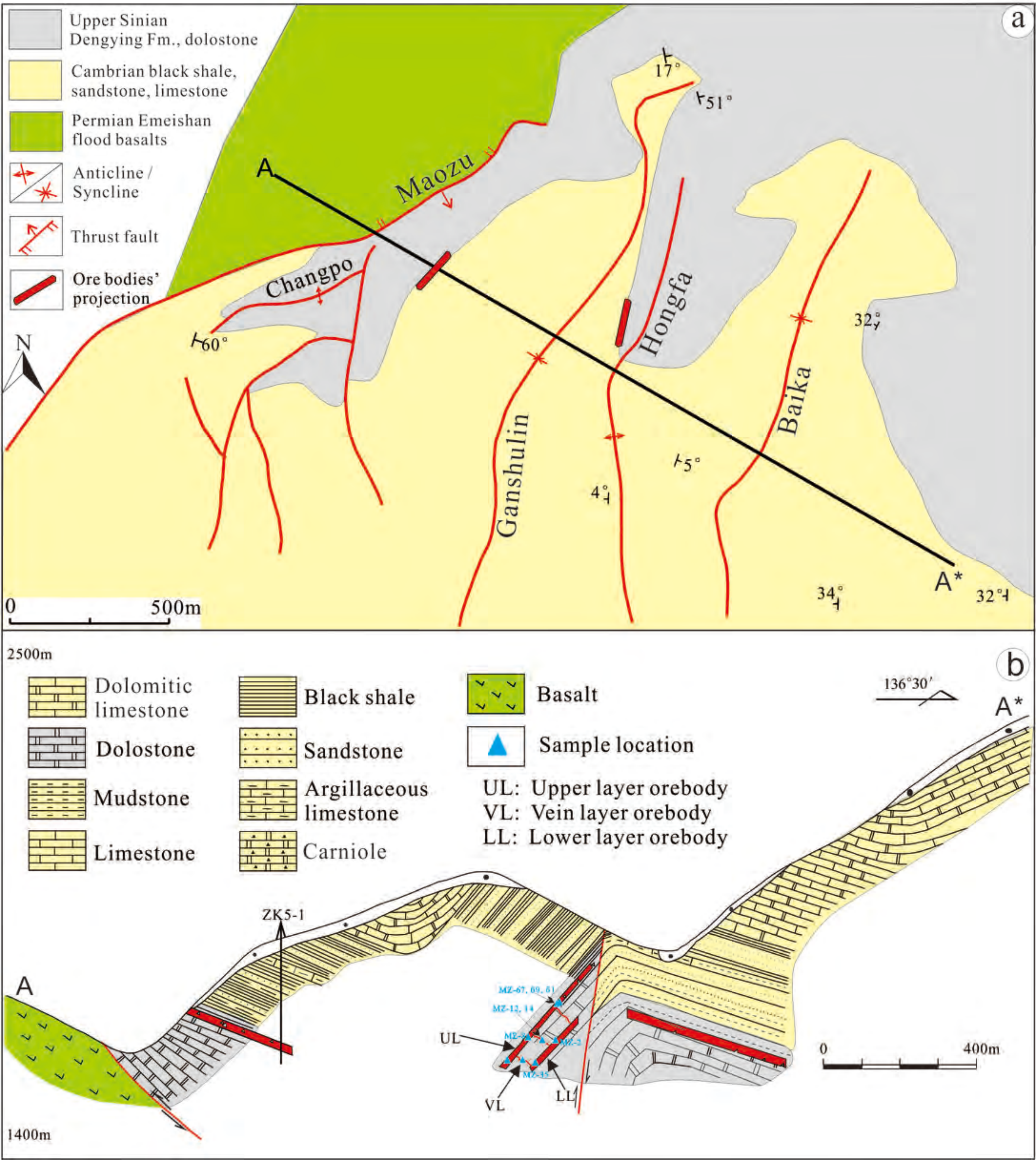
a
Upper Sinian Dengying Fm., dolostone
Cambrian black shale, sandstone, limestone
Permian Emeishan flood basalts
Anticline / Syncline
Thrust fault
Ore bodies' projection
N
A
A*
Maozu
Changpo
Hongfa
Ganshulin
Baika
17°
51°
60°
32°
5°
4°
34°
32°
0
500m
b
2500m
1400m
Dolomitic limestone
Dolostone
Mudstone
Limestone
Black shale
Sandstone
Argillaceous limestone
Carniole
Basalt
Sample location
UL: Upper layer orebody
VL: Vein layer orebody
LL: Lower layer orebody
136°30′
A*
A
ZK5-1
MZ-67, 69, 61
MZ-12, 14
MZ-8
MZ-2
MZ-35
UL
VL
LL
0
400m

Fig.4

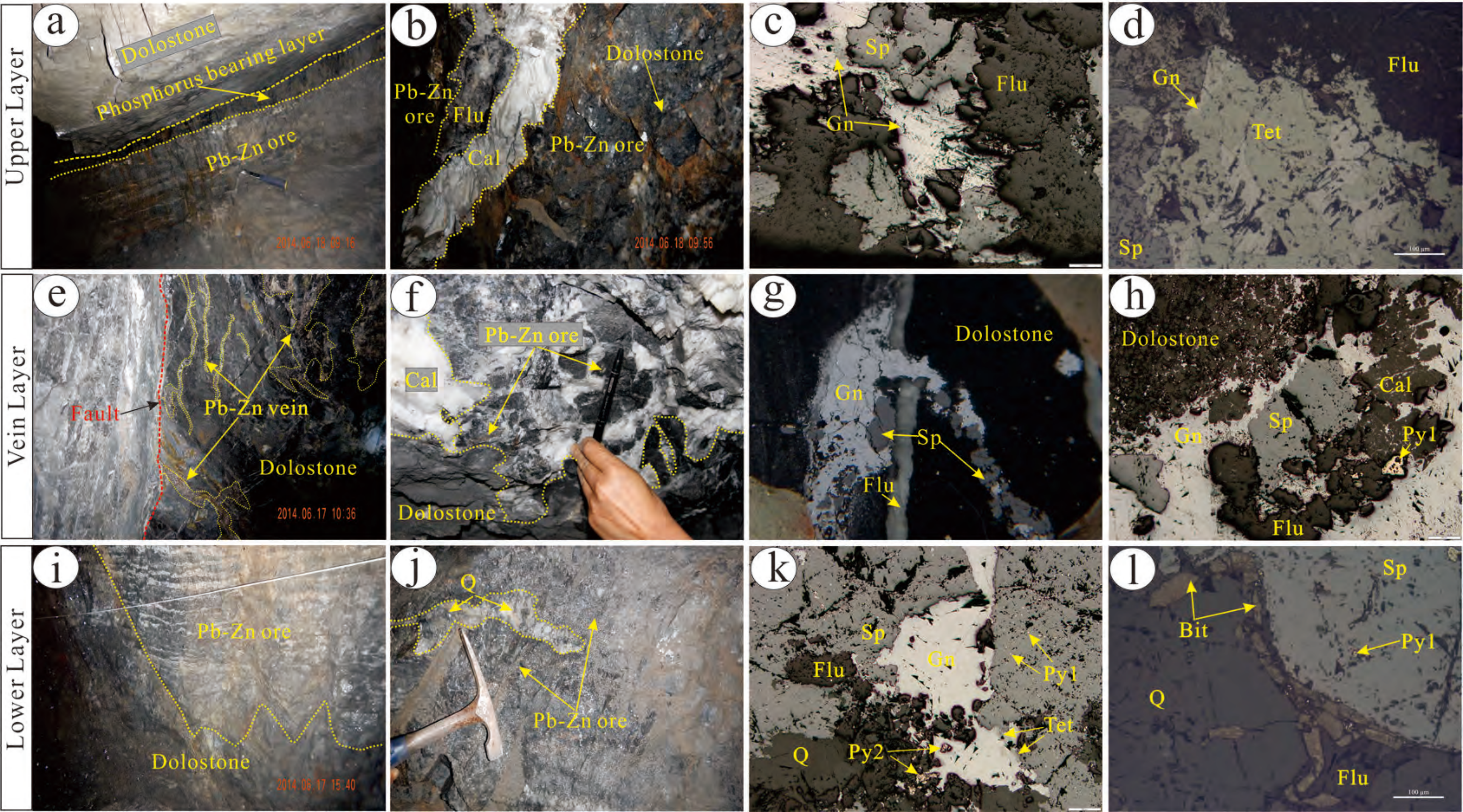
Upper Layer
Vein Layer
Lower Layer
a
Dolostone
Phosphorus bearing layer
Pb-Zn ore
2014.06.18 09:16
b
Pb-Zn ore
Flu
Cal
Dolostone
Pb-Zn ore
2014.06.18 09:56
c
Sp
Gn
Flu
d
Gn
Flu
Tet
Sp
100 μm
e
Fault
Pb-Zn vein
Dolostone
2014.06.17 10:36
f
Cal
Pb-Zn ore
Dolostone
g
Gn
Sp
Flu
Dolostone
h
Dolostone
Cal
Sp
Gn
Py1
Flu
i
Pb-Zn ore
Dolostone
2014.06.17 15:40
j
Q
Pb-Zn ore
k
Sp
Gn
Flu
Py1
Tet
Q
Py2
l
Sp
Bit
Py1
Q
Flu
100 μm

Fig.5

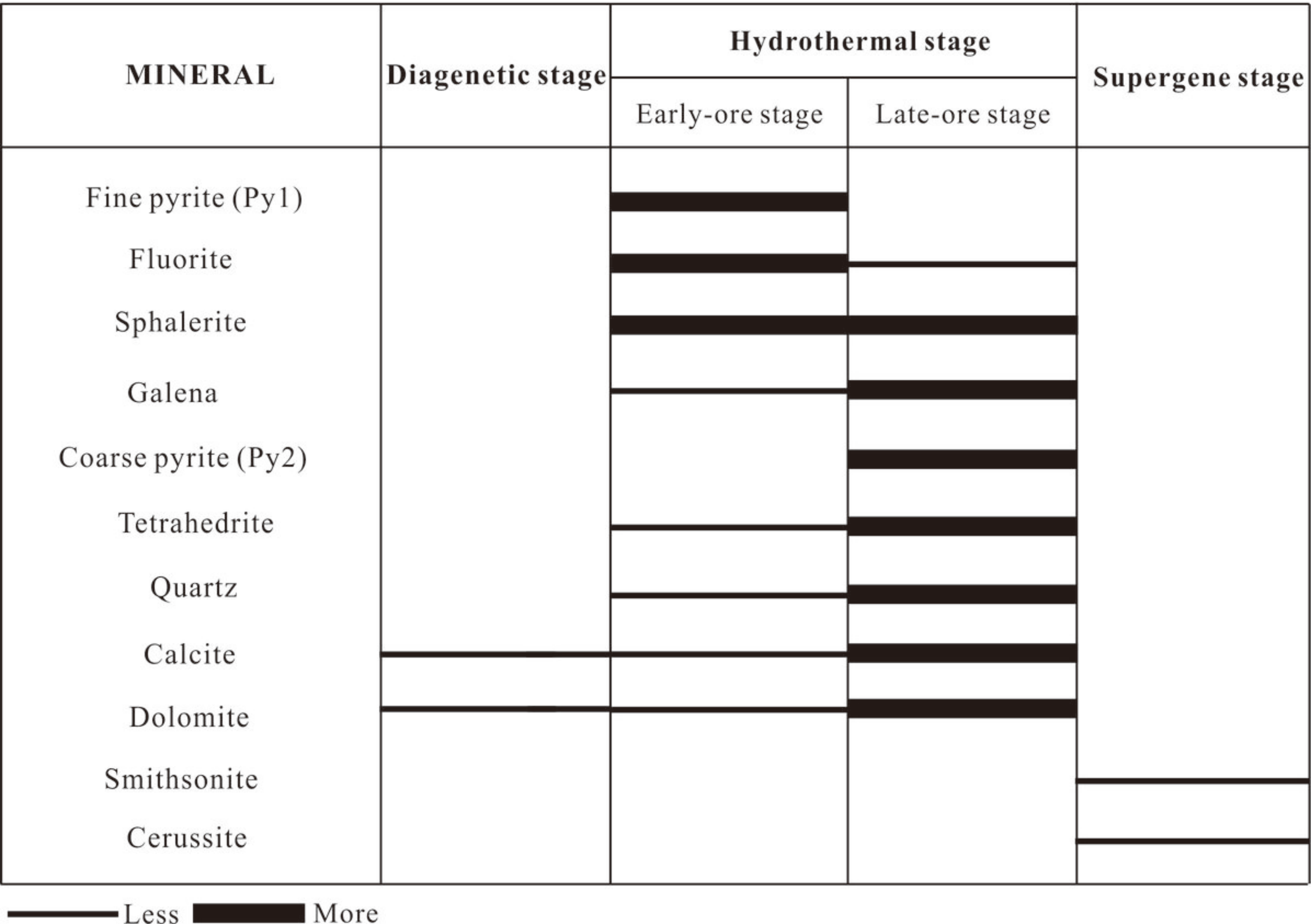
MINERAL
Diagenetic stage
Hydrothermal stage
Early-ore stage
Late-ore stage
Supergene stage
Fine pyrite (Py1)
Fluorite
Sphalerite
Galena
Coarse pyrite (Py2)
Tetrahedrite
Quartz
Calcite
Dolomite
Smithsonite
Cerussite
Less
More

Fig.6

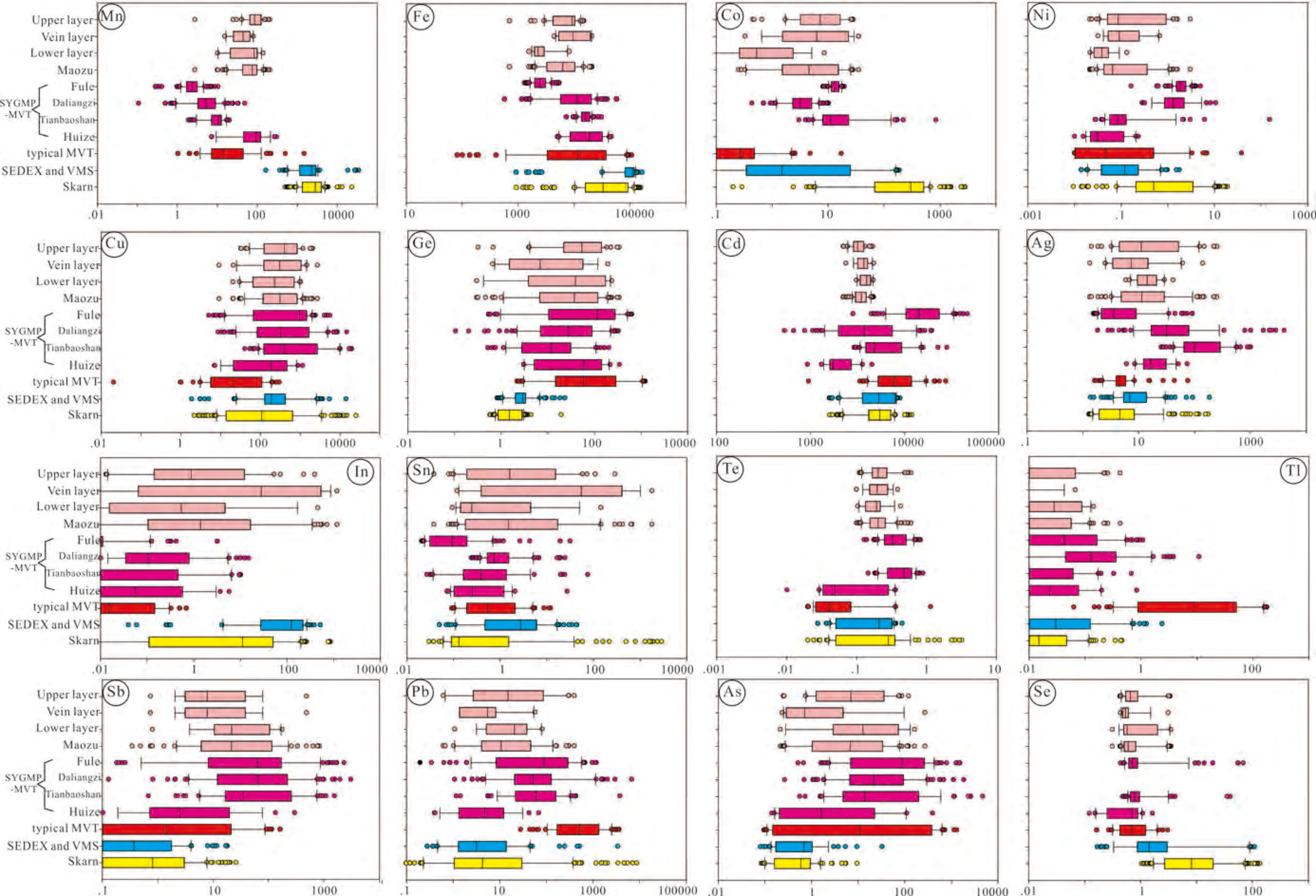
Upper layer
Vein layer
Lower layer
Maozu
Fule
Daliangzi
Tianbaoshan
Huize
SYGMP
-MVT
typical MVT
SEDEX and VMS
Skarn
Mn
.01
1
100
10000
Fe
10
1000
100000
Co
.1
10
1000
Ni
.001
.1
10
1000
Cu
.01
1
100
10000
Ge
.01
1
100
10000
Cd
100
1000
10000
100000
Ag
.1
10
1000
In
.01
1
100
10000
Sn
.01
1
100
10000
Te
.001
.01
.1
1
10
Tl
.01
1
100
Sb
.1
10
1000
Pb
.1
10
1000
100000
As
.01
1
100
10000
Se
.01
1
100

Fig.7

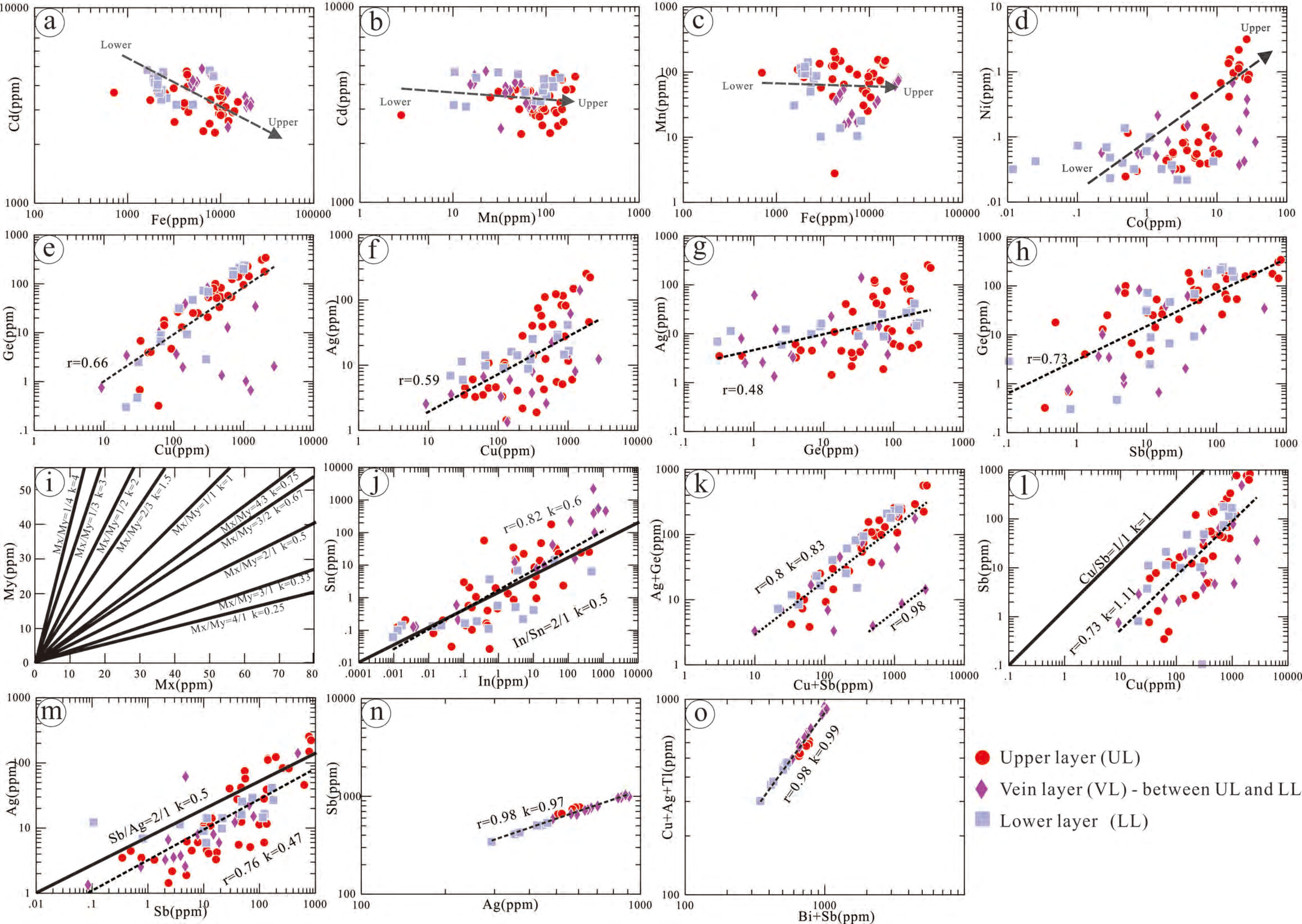
a
Lower
Upper
Cd(ppm)
Fe(ppm)
b
Lower
Upper
Cd(ppm)
Mn(ppm)
c
Lower
Upper
Mn(ppm)
Fe(ppm)
d
Upper
Lower
Ni(ppm)
Co(ppm)
e
r=0.66
Ge(ppm)
Cu(ppm)
f
r=0.59
Ag(ppm)
Cu(ppm)
g
r=0.48
Ag(ppm)
Ge(ppm)
h
r=0.73
Ge(ppm)
Sb(ppm)
i
Mx/My=1/4 k=4
Mx/My=1/3 k=3
Mx/My=1/2 k=2
Mx/My=2/3 k=1.5
Mx/My=1/1 k=1
Mx/My=4/3 k=0.75
Mx/My=3/2 k=0.67
Mx/My=2/1 k=0.5
Mx/My=3/1 k=0.33
Mx/My=4/1 k=0.25
My(ppm)
Mx(ppm)
j
r=0.82 k=0.6
In/Sn=2/1 k=0.5
Sn(ppm)
In(ppm)
k
r=0.8 k=0.83
r=0.98
Ag+Ge(ppm)
Cu+Sb(ppm)
l
Cu/Sb=1/1 k=1
r=0.73 k=1.11
Sb(ppm)
Cu(ppm)
m
Sb/Ag=2/1 k=0.5
r=0.76 k=0.47
Ag(ppm)
Sb(ppm)
n
r=0.98 k=0.97
Sb(ppm)
Ag(ppm)
o
r=0.98 k=0.99
Cu+Ag+Tl(ppm)
Bi+Sb(ppm)
● Upper layer (UL)
◆ Vein layer (VL) - between UL and LL
■ Lower layer (LL)

Fig.8

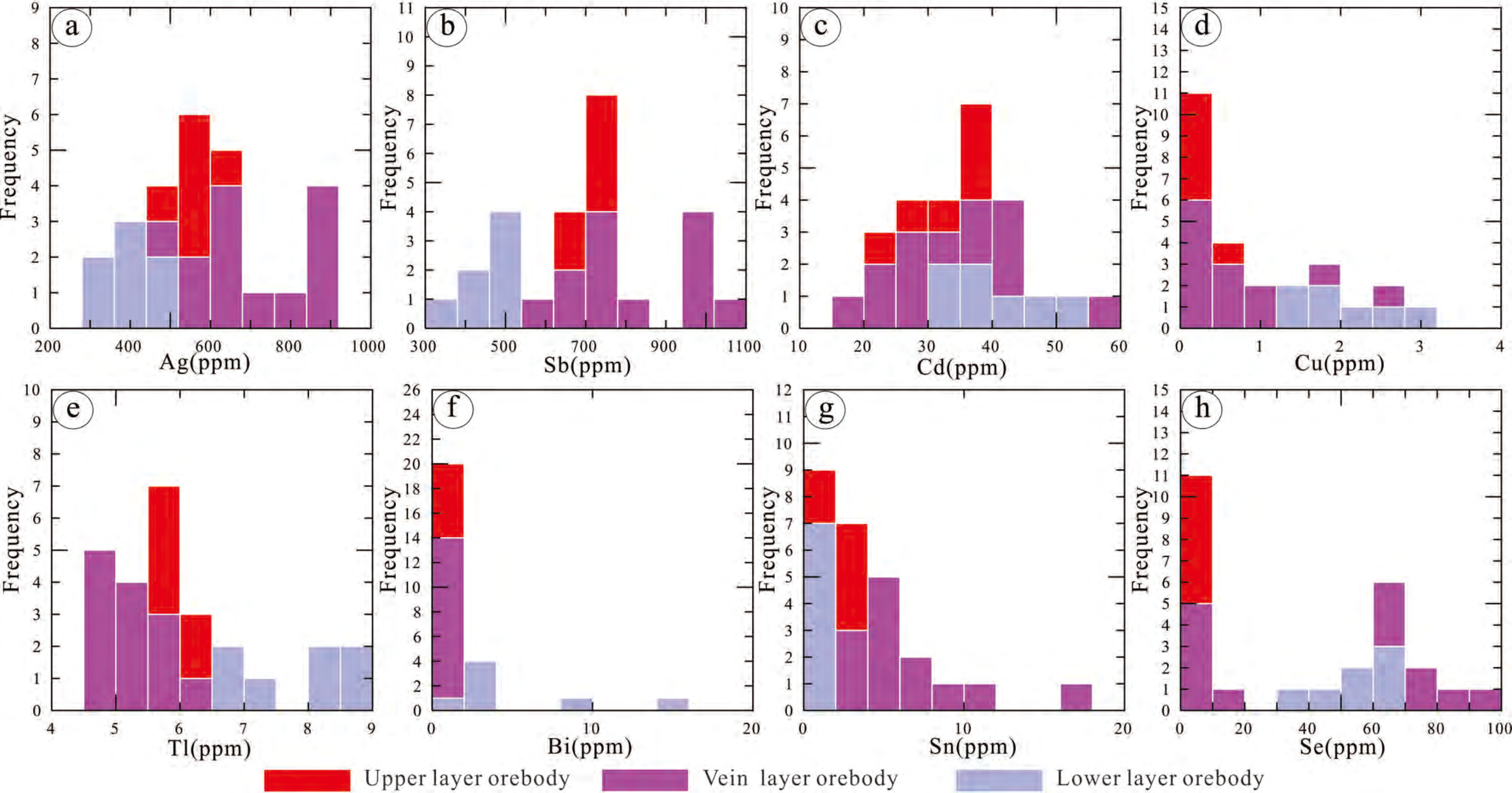
a
Frequency
Ag(ppm)
200
400
600
800
1000
b
Sb(ppm)
300
500
700
900
1100
c
Cd(ppm)
10
20
30
40
50
60
d
Cu(ppm)
0
1
2
3
4
e
Tl(ppm)
4
5
6
7
8
9
f
Bi(ppm)
0
10
20
g
Sn(ppm)
0
10
20
h
Se(ppm)
0
20
40
60
80
100
Upper layer orebody
Vein layer orebody
Lower layer orebody

Fig.9

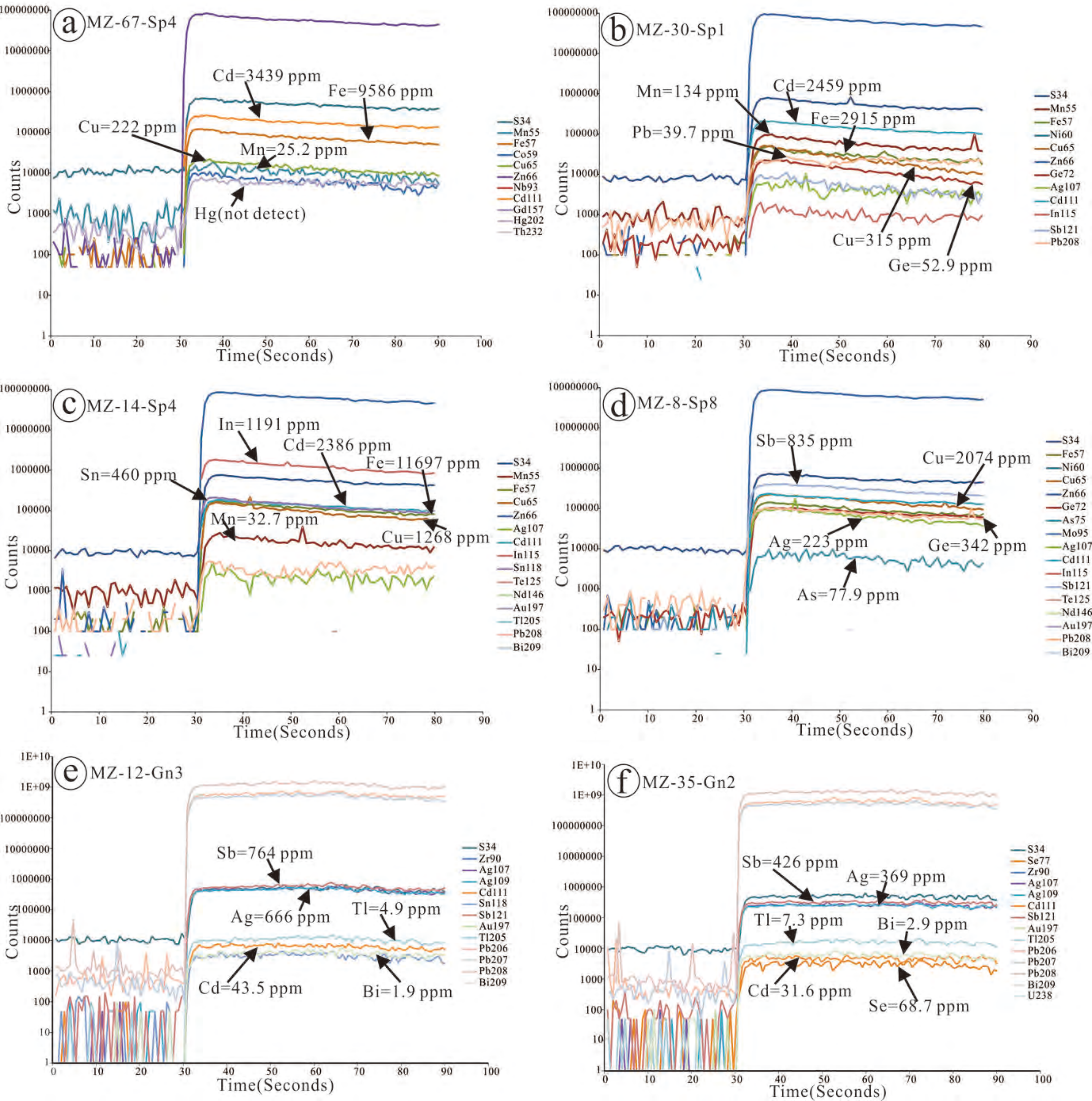
a
MZ-67-Sp4
Cd=3439 ppm
Fe=9586 ppm
Cu=222 ppm
Mn=25.2 ppm
Hg(not detect)
S34
Mn55
Fe57
Co59
Cu65
Zn66
Nb93
Cd111
Gd157
Hg202
Th232
b
MZ-30-Sp1
Mn=134 ppm
Cd=2459 ppm
Fe=2915 ppm
Pb=39.7 ppm
Cu=315 ppm
Ge=52.9 ppm
S34
Mn55
Fe57
Ni60
Cu65
Zn66
Ge72
Ag107
Cd111
In115
Sb121
Pb208
c
MZ-14-Sp4
In=1191 ppm
Cd=2386 ppm
Fe=11697 ppm
Sn=460 ppm
Mn=32.7 ppm
Cu=1268 ppm
S34
Mn55
Fe57
Cu65
Zn66
Ag107
Cd111
In115
Sn118
Te125
Nd146
Au197
Tl205
Pb208
Bi209
d
MZ-8-Sp8
Sb=835 ppm
Cu=2074 ppm
Ag=223 ppm
Ge=342 ppm
As=77.9 ppm
S34
Fe57
Ni60
Cu65
Zn66
Ge72
As75
Mo95
Ag107
Cd111
In115
Sb121
Te125
Nd146
Au197
Pb208
Bi209
e
MZ-12-Gn3
Sb=764 ppm
Ag=666 ppm
Tl=4.9 ppm
Cd=43.5 ppm
Bi=1.9 ppm
S34
Zr90
Ag107
Ag109
Cd111
Sn118
Sb121
Au197
Tl205
Pb206
Pb207
Pb208
Bi209
f
MZ-35-Gn2
Sb=426 ppm
Ag=369 ppm
Tl=7.3 ppm
Bi=2.9 ppm
Cd=31.6 ppm
Se=68.7 ppm
S34
Se77
Zr90
Ag107
Ag109
Cd111
Sb121
Au197
Tl205
Pb206
Pb207
Pb208
Bi209
U238
Counts
Time(Seconds)
1E+10
1E+09
100000000
10000000
1000000
100000
10000
1000
100
10
1
0
10
20
30
40
50
60
70
80
90
100

Fig.10

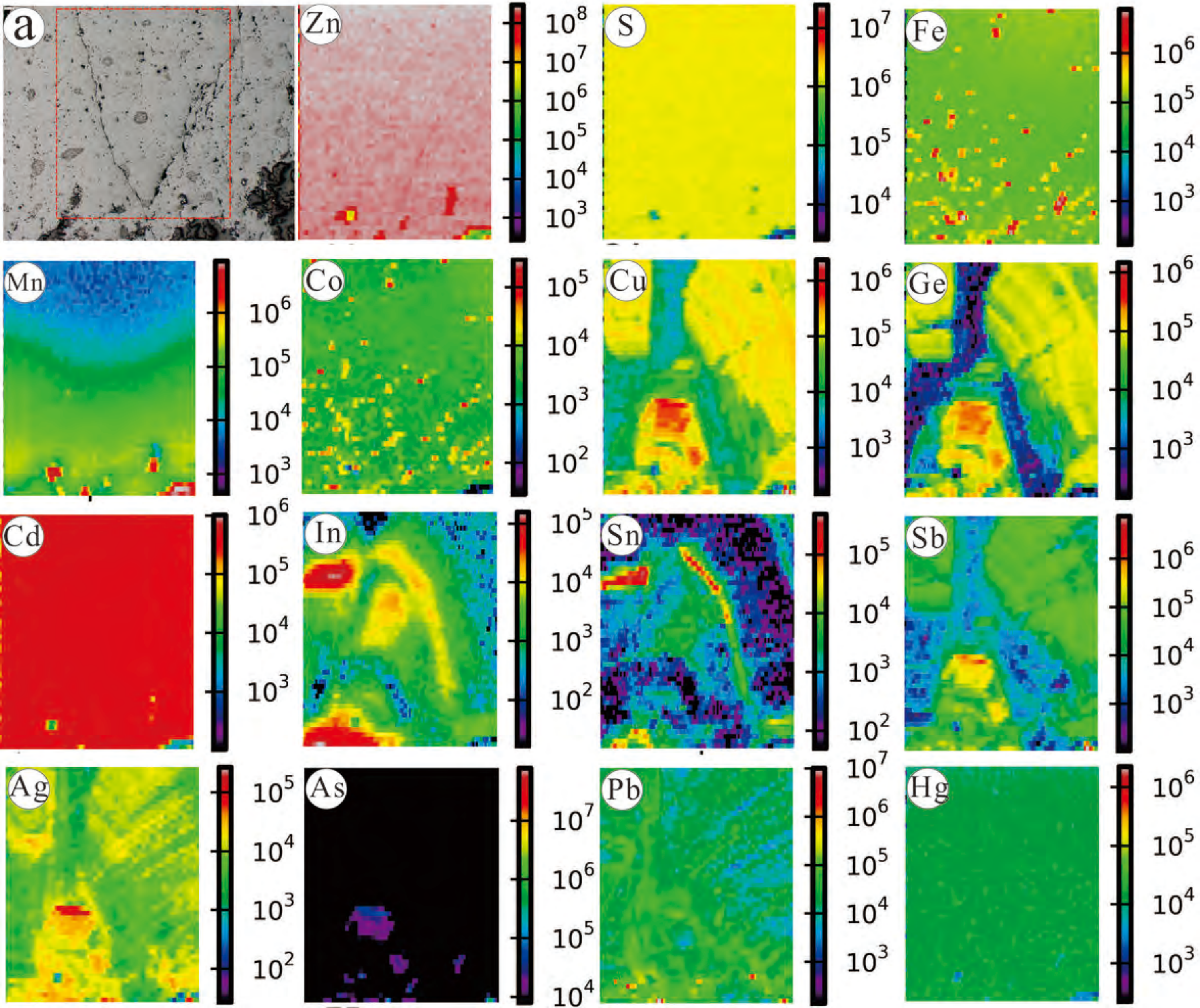
a
Zn
10^8
10^7
10^6
10^5
10^4
10^3
S
10^7
10^6
10^5
10^4
Fe
10^6
10^5
10^4
10^3
Mn
10^6
10^5
10^4
10^3
Co
10^5
10^4
10^3
10^2
Cu
10^6
10^5
10^4
10^3
Ge
10^6
10^5
10^4
10^3
Cd
10^6
10^5
10^4
10^3
In
10^5
10^4
10^3
10^2
Sn
10^5
10^4
10^3
10^2
Sb
10^6
10^5
10^4
10^3
Ag
10^5
10^4
10^3
10^2
As
10^7
10^6
10^5
10^4
Pb
10^7
10^6
10^5
10^4
10^3
Hg
10^6
10^5
10^4
10^3

Fig.12

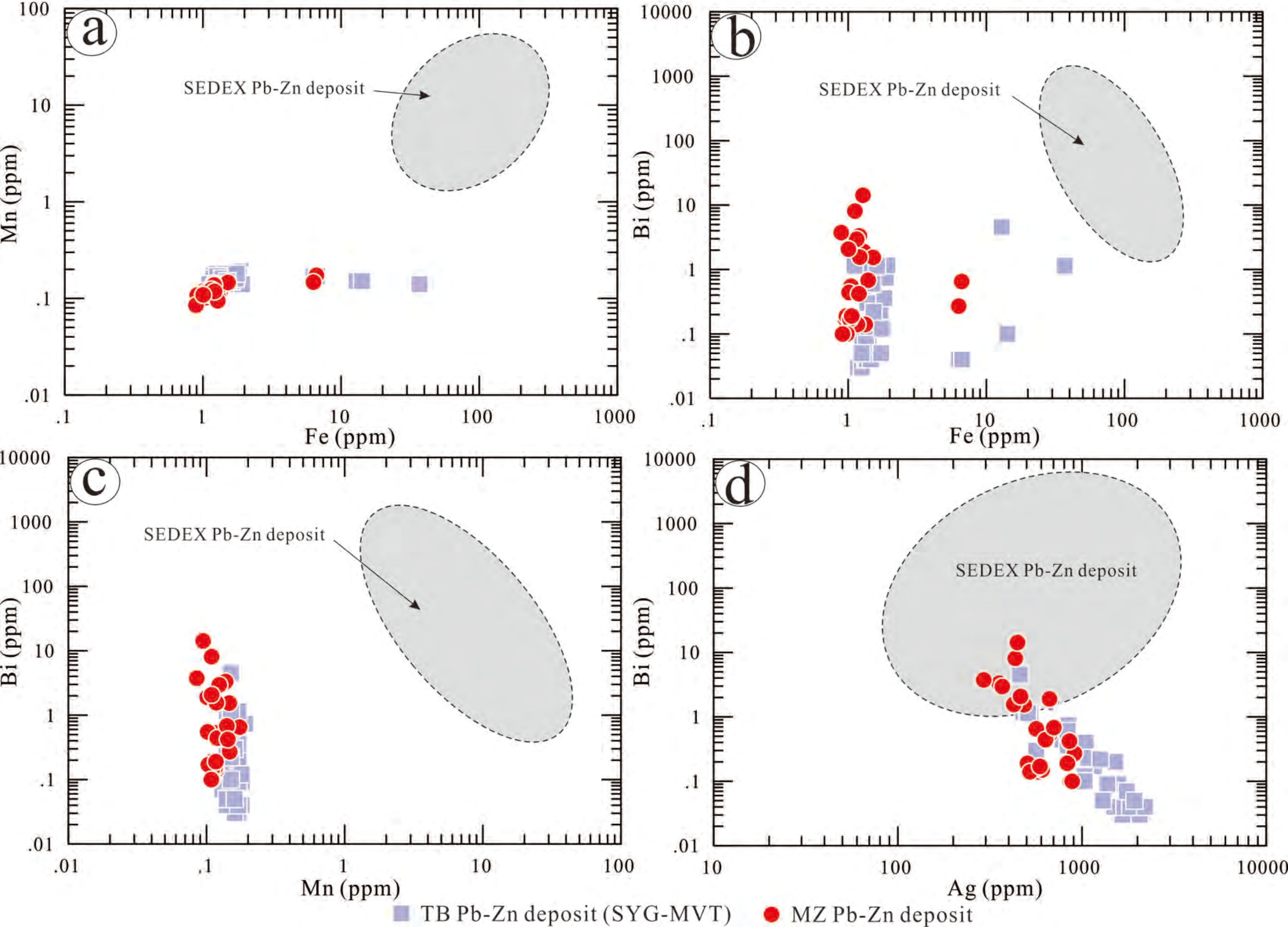
a
SEDEX Pb-Zn deposit
Mn (ppm)
100
10
1
.1
.01
Fe (ppm)
.1
1
10
100
1000
b
SEDEX Pb-Zn deposit
Bi (ppm)
10000
1000
100
10
1
.1
.01
Fe (ppm)
.1
1
10
100
1000
c
SEDEX Pb-Zn deposit
Bi (ppm)
10000
1000
100
10
1
.1
.01
Mn (ppm)
.01
.1
1
10
100
d
SEDEX Pb-Zn deposit
Bi (ppm)
10000
1000
100
10
1
.1
.01
Ag (ppm)
10
100
1000
10000
TB Pb-Zn deposit (SYG-MVT)
MZ Pb-Zn deposit

Fig.11

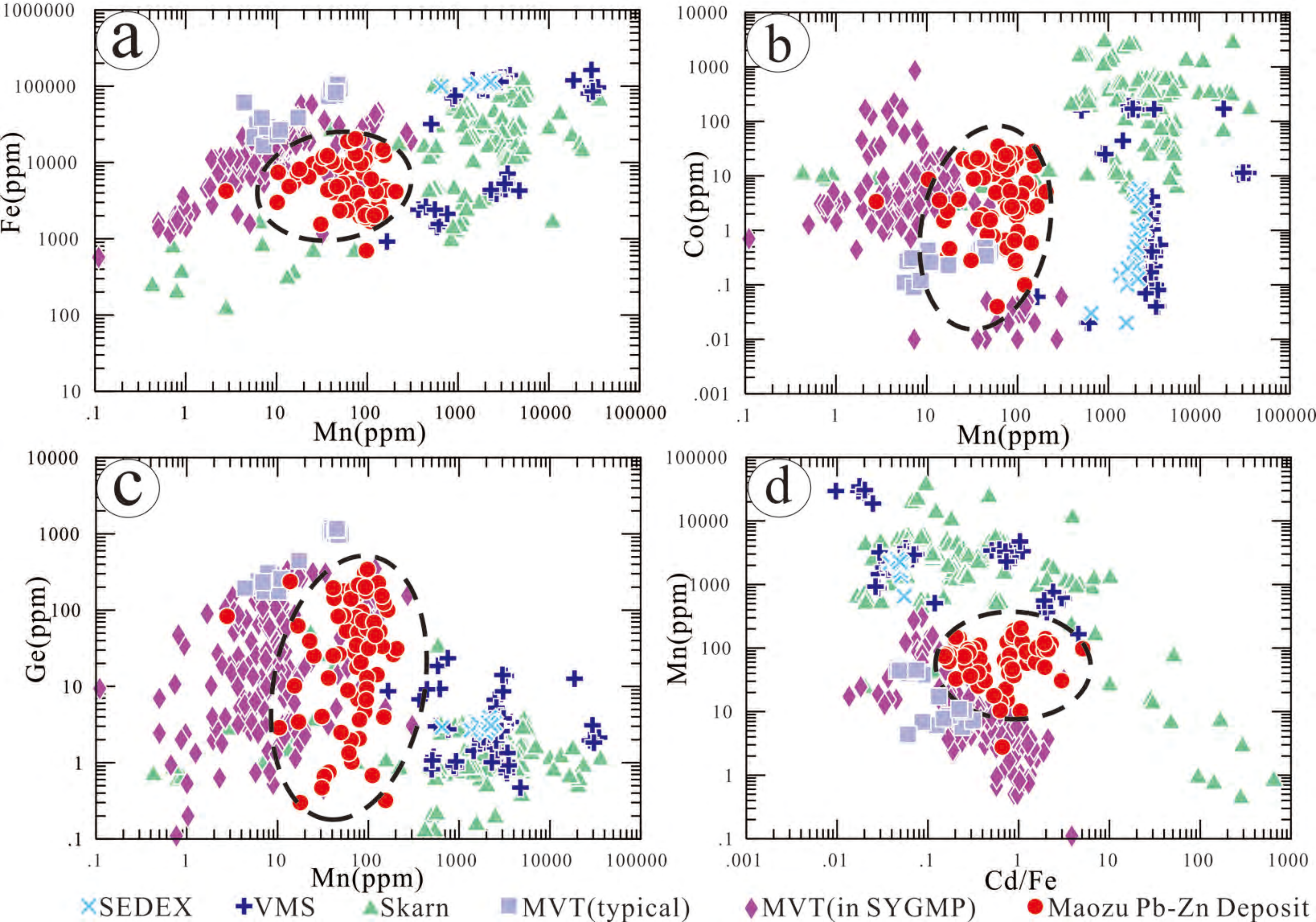
a
Fe(ppm)
1000000
100000
10000
1000
100
10
.1
1
10
100
1000
10000
100000
Mn(ppm)
b
Co(ppm)
10000
1000
100
10
1
.1
.01
.001
.1
1
10
100
1000
10000
100000
Mn(ppm)
c
Ge(ppm)
10000
1000
100
10
1
.1
.1
1
10
100
1000
10000
100000
Mn(ppm)
d
Mn(ppm)
100000
10000
1000
100
10
1
.1
.001
.01
.1
1
10
100
1000
Cd/Fe
SEDEX
VMS
Skarn
MVT(typical)
MVT(in SYGMP)
Maozu Pb-Zn Deposit